Exotic toroidal and superdeformed configurations in light atomic nuclei: Predictions using a mean-field Hamiltonian without parametric correlations

A. Gaamouci,[1] I. Dedes,[2,3] J. Dudek,[3,4] A. Baran,[3] N. Benhamouda,[1] D. Curien,[4] H. L. Wang,[5,4] and J. Yang[3]

[1]*Laboratoire de Physique Théorique, Faculté de Physique, USTHB, BP 32, El Alia, 16111 Bab Ezzouar, Algiers, Algeria*

[2]*Institute of Nuclear Physics Polish Academy of Sciences, PL-31 342 Kraków, Poland*

[3]*Institute of Physics, Marie Curie-Skłodowska University, PL-20 031 Lublin, Poland*

[4]*Université de Strasbourg, CNRS, IPHC UMR 7178, F-67 000 Strasbourg, France*

[5]*School of Physics and Microelectronics, Zhengzhou University, Zhengzhou 450001, China*

(Received 31 December 2020; revised 11 April 2021; accepted 6 May 2021; published 19 May 2021)

Mean-field calculations in multidimensional deformation spaces are performed and the shape coexistence and isomers generated by exotic nuclear configurations and toroidal and superdeformed ones are addressed. We use a phenomenological mean-field Hamiltonian of Woods-Saxon type with its universal parametrization involving eight parameters fixed once for all for the full periodic table. Original parametric correlations existing in this type of Hamiltonians are removed using methods of inverse problem theory of applied mathematics. Stochastic analysis of uncertainties of the final nuclear energy predictions with the obtained correlation-free parametrization is performed and the viability tests are illustrated and discussed. Prediction capacities of resulting model related to the description of the nuclear shape properties are cross-checked using the experimental information available, revealing full coherence. Presented results encourage experimental verification of predicted exotic structures; suggestions related to identification possibilities are formulated and discussed.

DOI: 10.1103/PhysRevC.103.054311

I. INTRODUCTION

The notions of shape coexistence and of exotic shapes in atomic nuclei have long traditions in nuclear structure literature even though, especially the issue of exotic shapes, underwent a significant evolution in view of the progress in a more recent research of exotic nuclei. It is worth emphasizing that nuclear shapes in general and the exotic ones in particular are ultimately related to the symmetry properties of the nuclear mean-field Hamiltonian, which are at the very basis of their understanding.

At the most general level of the symmetry discussion, one may evoke the unitary group, U(n), and the implied symmetries at the many-body level of the description of the nuclear systems followed by the formal subgroup chains which lead, at certain stage, to the symmetries such as, e.g., SU(3) and pseudo-SU(3), down to the point groups describing geometrical aspects of the symmetry—to mention just a few selected keywords on the longer list. In particular, it has been pointed out in Refs. [1,2], that SU(3) appears as an elementary symmetry of the nuclear shell model, with the consequences that the underlying Hamiltonians combine the independent particle picture with collective rotation and/or collective effects induced by the quadrupole-quadrupole interactions inherent to the SU(3) generator structure. Nuclear structure mechanisms discussed in this article can be seen as manifestations of group-chain generated symmetries and symmetry-breaking phenomena. They can be studied via nuclear structure concepts such as single nucleon energies, total potential energies, and implied noncollective phenomena, e.g., in the form of K isomers built on axial-symmetry configurations or collective effects, as, e.g., collective vibrations or nuclear rotational bands built on various nonspherical-equilibrium configurations.

Historically, one of the first nuclear geometries which was considered unusual—thus exotic in the context of the present article—was associated with very elongated axial symmetry (ellipsoidal) shapes with the axis ratio approaching 2:1. The latter became of particular interest with the arrival of the first experimental discoveries of fission isomers and the underlying, so-called double-hump fission barriers. Interested readers may consult an early review in Ref. [3] for this part of the evolution. The focus on this particular geometry has been strengthened by the discovery of the nuclear superdeformation at high angular momenta in ^{152}Dy nucleus, first evidence in Ref. [4], one year after the theory predictions based on the nuclear mean-field approach with the cranking approximation, Fig. 2 of Ref. [5]. Numerous other cases of superdeformation at high spins were found experimentally in many other nuclei in the following years.

In the meantime, an adaptation of the original SU(3) considerations to the description of relatively heavy nuclei gave rise to introducing the so-called pseudo-SU(3) symmetry group, Refs. [6–9], which was known already at the time of the first superdeformation discovery. The pseudo-SU(3) symmetry considerations have been applied, cf. Figs. 1 and 2 of Ref. [10], to predict dozens of yet unknown

 ©2021 American Physical Society

superdeformation cases and equally significantly to predict the nuclei in which this mechanism was *not* expected to take place. These predictions were fully confirmed experimentally during the years to come both in terms of the presence and absence of superdeformed configurations in agreement with predictions, cf. Ref. [11] and references therein. This discussion, focused on superdeformed nuclear configurations, strongly accentuates the importance of the symmetry arguments in construction of the modeling methods with manifested predictive power.

Early model arguments evoked in interpreting quantum effects behind the superdeformation employed shell structures produced by a deformed harmonic oscillator. Introducing axially symmetric harmonic-oscillator (HO) with frequency ω_3 representing particle oscillations along the $\mathcal{O}_3$ axis and $\omega_\perp$ representing oscillations in the directions perpendicular to $\mathcal{O}_3$, one demonstrates directly (cf. Figs. 6–48 in Ref. [12]) that for frequency ratios satisfying $\omega_\perp : \omega_z = 2 : 1$, the HO eigenvalues form specific degeneracies at certain energies with strong gaps in between. As is well known today, strong gaps in the single-particle spectra imply an increase in nuclear binding, via strong negative so-called shell (or shell-correction) contributions to the total nuclear energies and thus a possible appearance of secondary, ternary, etc., potential energy minima, leading to various forms of shape coexistence.

Following the same search principles, an "inverted" harmonic oscillator frequency ratio $\omega_\perp : \omega_z = 1 : 2$, rather than 2:1, another series of degeneracies of the oscillator single-particle levels is obtained favoring strongly deformed *oblate* shape configurations with the shell gaps differing from those associated with the prolate shapes, thus encouraging the research of "superoblate" nuclear deformations. In this article, we focus on relatively light nuclei approximately in the mass range $A \approx (30–50)$. Many of them attracted attention from both theoretical and experimental viewpoints in the past. While selected aspects of the experimental progress will be pointed out in the article, here let us mention the arguments of Ref. [13] suggesting possibly significant oblate-shape shell -effects at $Z, N = 14, 28, 36$. Significantly earlier, Ref. [14], experimental arguments based on the in-beam spectroscopy and fragmentation reaction methods were obtained in favor of very strong gaps at $N = 14$ and $N = 16$; cf. also Fig. 9 in Sec. V.

We will discuss and illustrate in particular exotic nuclear shape coexistence and competition, likely leading to isomers which can be used to identify such structures. We believe that exotic symmetries and isomers generated by them are going to strongly impact our studies of nuclear structure and influence experimental and instrumental methods leading to their manifestations. We will show that, in particular at the large gaps in the single-nucleon spectra produced by the strongly oblate *quadrupole*-deformed configurations the underlying gaps can even be strengthened by superposing higher order multipole deformations, such as the hexadecapole one, $\alpha_{\lambda=4,\mu}$. Among the latter ones, a significant impact from the extremely large axial symmetry α_{40} deformation is shown to lead to yet another exotic class of shapes resembling closely the toroidal structures as discussed in detail below.

The latter exotic structures may parallel the recently identified tetrahedral and octahedral (so-called high-rank) symmetries in subatomic physics, Ref. [15], predicted to generate rotational bands, yet with neither electric quadrupole nor dipole transitions populating or depopulating those band-member states. Thus, the lowest order electromagnetic-decay transitions allowed are of the order of $\lambda = 3$ (octupole) or $\lambda = 4$ (hexadecapole), implying hindrance of several orders of magnitude. For all these reasons, identification of the high-rank symmetries remains challenging; they are sometimes referred to as hidden symmetries. It is worth emphasizing that because of the high-rank symmetry hindrance, rotational bands in question are composed of isomers, the latter detectable with the help of the modern high-resolution mass-spectrometry methods. Thus, the mass spectrometry can be seen as an encouraging technique of detection of both toroidal and high-rank symmetry isomers.

II. NUCLEAR ENERGY MODELING: TECHNIQUES AND RELATED CHALLENGES

We employ the macroscopic-microscopic method using phenomenological realization of the nuclear mean-field Hamiltonian with the deformed Woods-Saxon potential. We follow the concept of the "universal parametrization" introduced by other authors, Ref. [16], according to which one single set of parameters of such a Hamiltonian is applicable to all nuclei within the mass table. This idea has been in use over many years and numerous application examples can be found in contemporary literature as illustrated, e.g., in Ref. [17].

A. Mean-field Hamiltonian and total nuclear energy: Calculation technique

Our numerical calculations are performed with the standard nuclear mean-field Woods-Saxon Hamiltonian:

$$\hat{H} = \hat{T} + \hat{\mathcal{V}}_{\rm WS} + \hat{\mathcal{V}}^{\rm so}_{\rm WS} + [\hat{\mathcal{V}}_{\rm Coulomb} \text{ for protons}]. \quad (1)$$

Above, $\hat{T}$ represents kinetic energy operator and $\hat{\mathcal{V}}_{\rm WS}$ is the central Woods-Saxon potential,

$$\hat{\mathcal{V}}_{\rm WS}(\vec{r}, \alpha; V^{\rm c}, r^{\rm c}, a^{\rm c}) = \frac{V^{\rm c}}{1 + \exp[{\rm dist}_\Sigma(\vec{r}, R^{\rm c}; \alpha)/a^{\rm c}]}, \quad (2)$$

where $V^{\rm c}$ denotes the central potential depth parameter and $r^{\rm c}$ in $R^{\rm c} = r^{\rm c}A^{1/3}$ is the central radius parameter. Similarly $a^{\rm c}$ is referred to as central diffusivity parameter. Position-vector-dependent function ${\rm dist}_\Sigma(\vec{r}, R^{\rm c}; \alpha)$ is defined as the geometrical distance between current point position in space, $\vec{r} \equiv \{x, y, z\}$, and the nuclear surface Σ. The latter is represented in terms of the spherical-harmonic basis expansion as

$$\Sigma: \quad R(\vartheta, \varphi) \equiv C(\alpha) R^{\rm c} \left[1 + \sum_\lambda \sum_\mu \alpha_{\lambda\mu} Y_{\lambda\mu}(\vartheta, \varphi) \right], \quad (3)$$

where ensemble of all the deformation parameters used, $\{\alpha_{\lambda\mu}\}$, is abbreviated to α. Above, $C(\alpha)$ assures the constant volume condition, i.e., the property that the volume enclosed by Σ is independent of the actual shape and equal to the volume of the corresponding spherical nucleus.

The spin-orbit potential is defined as usual as

$$\hat{V}^{\rm so}_{\rm WS}(\vec{r},\,\hat{p},\hat{s},\alpha;\lambda^{\rm so},r^{\rm so},a^{\rm so}) = \frac{2\hbar\lambda^{\rm so}}{(2mc)^2}\left[\left(\vec{\nabla}V^{\rm so}_{\rm WS}\right)\wedge\hat{p}\,\right]\cdot\hat{s}, \tag{4}$$

where

$$V^{\rm so}_{\rm WS}(r,\alpha;V^{\rm c},r^{\rm so},a^{\rm so}) = \frac{V^{\rm c}}{1+\exp[{\rm dist}_\Sigma(\vec{r},R^{\rm so};\alpha)/a^{\rm so}]}. \tag{5}$$

By convention, $\lambda^{\rm so}$ is a dimensionless spin-orbit strength-scaling factor, $r^{\rm so}$ in $R^{\rm so}=r^{\rm so}A^{1/3}$ is the spin-orbit radius, and $a^{\rm so}$ is the spin-orbit diffusivity-parameter.

This traditional definition of the deformed Woods-Saxon potentials and Hamiltonian depends on two sets of six parameters each,

$$\left\{V^{\rm c}_{\pi,\nu},\,r^{\rm c}_{\pi,\nu},\,a^{\rm c}_{\pi,\nu};\lambda^{\rm so}_{\pi,\nu},\,r^{\rm so}_{\pi,\nu},\,a^{\rm so}_{\pi,\nu}\right\}, \tag{6}$$

one for protons, π, and one for neutrons, ν, respectively. The issues of parameter optimization, parametric correlations, prediction capacities, and stabilization are addressed in the following sections.

Schrödinger equation with the Hamiltonian of Eq. (1) is solved using standard diagonalization methods employing matrix representations of the Hamiltonian with Cartesian harmonic oscillator (HO) basis. We introduce broad nuclear deformation ranges trying to assure in this way that all the low-lying potential energy minima which compete energetically are taken care of, including shapes referred to as prolate or oblate hyperdeformed. Employing such broad shape variations imposes relatively severe constraints on the adaptation of the harmonic oscillator basis in order to assure the stability of the final results. We consider basis choice acceptable if at any deformation point the least bound nucleonic levels vary with the variation in the basis cutoff not stronger than at the third decimal place.

To achieve the required stability of the mean-field solutions, we introduce the HO basis cutoff parameter $N_{\rm max}$; we also allow for anisotropy of the HO potential. The anisotropy is controlled with the help of three harmonic oscillator frequencies (ω_x, ω_y, ω_z) adjusted as usual by maximizing the volume overlap between the deformed potential and the deformed basis. We have verified that with $N_{\rm max}=18$, i.e., with 1330 HO states contained in $N\leqslant 18$ HO main shells, we arrive at stabilizing all of the few dozens of the nucleonic bound states according to the criterion specified above for all nuclei and at all deformations considered in this article.

Total nuclear energies are calculated according to the standard macroscopic-microscopic method of Strutinsky, Ref. [18], as

$$E_{\rm total} = E_{\rm macro} + \delta E^{\pi}_{\rm micro} + \delta E^{\nu}_{\rm micro}, \tag{7}$$

where the first term represents the classical macroscopic liquid-drop model contribution and each of the microscopic terms have the form of the sums of the so-called shell correction, Ref. [18], and pairing correction terms.

In this article, macroscopic energy realization known as finite-range liquid-drop model (FRLDM) is chosen. It contains the so-called modified surface-energy term given by the Yukawa-plus-exponential finite-range model of Ref. [19] within the formulation of Refs. [20,21]. The final macroscopic energy expression used here coincides with Eq. (62) of Ref. [22].

Whereas Strutinsky shell-correction energy expression is used in the majority of published articles in the form which can be considered standard, cf., e.g., Eq. (8) of Ref. [23], the latter one used also by us, the pairing-energy contribution in Eq. (7), appears in the literature in a number of phenomenological variants as a part of the microscopic-energy term

$$\delta E_{\rm micro} = \delta E_{\rm shell} + \delta E_{\rm pairing}. \tag{8}$$

Even though the pairing energy expressions can also be considered as well established and used by various authors, the existence of various variants may render confusions likely. To avoid the danger, we provide here the minimum precision without attempting any review-type descriptions.

It is fair to say that four types of the phenomenological pairing energy expressions dominate in the applications of the macroscopic-microscopic approach. They are usually referred to as *pairing correlation* and *pairing correction* energies. Both may appear in realizations employing (or not employing) particle number projection technique within Bardeen-Cooper-Schrieffer (BCS) formulation of the nuclear monopole-pairing problem. It follows that any of the four terms below,

$$\delta E_{\rm pairing} \leftrightarrow \delta E_{\rm correc},\ \delta E_{\rm correl},\ \delta E^{\rm PNP}_{\rm correc},\ \delta E^{\rm PNP}_{\rm correl}, \tag{9}$$

may appear as an acceptable alternative in place of $\delta E_{\rm pairing}$ in Eq. (8), assuring nearly the same predictions.

These pairing energy expressions are simplest to present beginning with *pairing correlation* term defined as the difference between BCS energy of the system at "paired solution" (pairing $\Delta\neq 0$) and its partner expression corresponding to "no-pairing solution" ($\Delta=0$):

$$\delta E_{\rm correl} = \underbrace{\sum_{\nu=1}^{N_p}\left(2\epsilon_\nu v_\nu^2 - G v_\nu^4\right) - \frac{\Delta^2}{G}}_{\Delta\neq 0} - \underbrace{\sum_{\nu=1}^{N_p/2}(2\epsilon_\nu - G)}_{\Delta=0}, \tag{10}$$

according to standard definitions and notation; cf. Eq. (9) of Ref. [23] for details. Construction of the *pairing-correction* term can be seen as analogous to Strutinsky *shell-correction* term. It is defined as the *difference* between the nuclear single-particle contribution and the corresponding "average" or "smoothed out" image. The corresponding pairing-correction partner expression is defined as the difference between the one above and its Strutinsky-type smoothed out partner; interested readers will find all details in Sec. V C of Ref. [23].

In our project, we calculate the nuclear energies according to all the four variants in Eq. (9), thus controlling the possible differences implied by the physicist's arbitrary choice of a phenomenological variant. Our calculations for all the nuclei in the considered mass range and all deformations show that the total energy results remain in excellent structural correspondence, the differences being very well approximated by small constants shifts. In what follows, we limit our illustrations to the pairing-correction variant.

The microscopic total energy expression depends on two terms in the full Hamiltonian: the mean-field term, Eq. (1), with parameters listed in Eq. (6), which describe the single-nucleon energies, and the monopole pairing Hamiltonian,

$$\hat{H}_{\text{pair.}} = -G \sum_{\mu\nu} c_\nu^+ c_{\bar{\nu}}^+ c_{\bar{\mu}} c_\mu, \tag{11}$$

following the standard definition and notation, the latter depending on the so-called pairing-strength constant, $G \leftrightarrow G_\pi$ or G_ν, for protons and neutrons, respectively. Functioning of $\hat{H}_{\text{pair}}$ can be controlled experimentally via BCS pairing gaps, Δ, with the help of the nuclear binding energies using the double difference expression:

$$\Delta^{(3)}(N) \equiv \frac{(-1)^N}{2}[B(N-1) + B(N+1) - 2B(N)], \tag{12}$$

with $B(N)$ denoting the (negative) binding energy of the system with N particles; cf. Eq. (1) in Ref. [24]. Indeed, one can argue that for odd-N we have, approximately, $\Delta^{(3)}(N) \approx \Delta_{\text{qp}} \approx \Delta$, where Δ_{qp} is the lowest quasiparticle energy and Δ is the BCS paring gap energy. Thus, extracting the experimental information about Δ, from now on referred to as Δ_{exp}, we have adjusted pairing strengths in such a way that $\Delta_{\text{exp}} \approx \Delta_{\text{BCS}}$ at the ground-state equilibrium deformations; see below.

In the present project, the strength constants G are treated with the help of a simplified but proven realistic prescription

$$\frac{1}{G} = \bar{\rho} \ln \left\{ \left[\left(\frac{N_p}{2\bar{\rho}\bar{\Delta}} \right)^2 + 1 \right]^{1/2} + \frac{N_p}{2\bar{\rho}\bar{\Delta}} \right\} \tag{13}$$

of Ref. [23]. According to the latter reference, N_p is the number of pairs taken when solving the BCS equations, whereas $\bar{\rho}$ and $\bar{\Delta}$ are, respectively, the average density of levels at the Fermi level treated with the help of the Strutinsky prescriptions and $\bar{\Delta}$ is the so-called average pairing Δ, in the past usually approximated by an average empirical trend with $\bar{\Delta} = 12\,\text{MeV}/\sqrt{A}$. Interested readers will find the relevant details in the text preceding Eq. (13) in Ref. [23].

To assure possibly realistic phenomenological prescription for the pairing strength constants, we performed the calculations for all the even-even nuclei with $14 \leqslant Z \leqslant 46$ for $\alpha_{20} \in [-0.6, +0.6]$ and $\alpha_{22} \in [-0.4, +0.4]$ [for reasons of compatibility with the point-group theory symmetry requirements, we are not using the (β, γ) notation at the level of the mesh definitions] and $\alpha_{40} \in [-0.3, +0.3]$. We arrive at reproducing the criterion of the correspondence $\Delta_{\text{BCS}}^{\text{equil}} \approx \Delta_{\text{exp}}$ at the ground-state equilibrium deformations for the great majority of the nuclei for which Δ_{exp} can be extracted in the considered mass region with the discrepancies of the order of ± 100 keV by replacing the constant of 12 MeV in $\bar{\Delta}$ above by $\alpha_Z = 11.2$ MeV and $\alpha_N = 9.1$ MeV for protons and neutrons, respectively.

B. Inverse problem, parametric correlations, and their impact on modeling uncertainties

Inverse problem theory belongs to the most actively developing fields of *applied mathematics* today. It enters various domains of applied research, information, and statistics, as well as estimates of modeling uncertainties in physics and some branches of fundamental research. An interested reader will find subjects of importance in specialized journals of inverse problem theory, Ref. [25], or monographs such as Refs. [26–30], and many others.

There is an increasing number of publications which address the issues of modeling uncertainties and statistics and which focus specifically on nuclear physics. However, reviewing this evolution here would go beyond the scope of the present article. Recurrent related issues of actuality can be found, e.g., in Refs. [31–33] and references therein. Below we limit ourselves to reminding the reader about a few standard notions from vocabulary of the inverse problem theory, focusing on the issue of parametric correlations and their relation to prediction uncertainties. Rather extensive elementary-level discussion linking the nuclear many-body problem with the inverse-problem theory methods can be found in Ref. [34].

In applied mathematics, it is customary to use a single symbol $\hat{\mathcal{M}}$ representing, e.g., a physical model, which depends on adjustable parameters $\{p_1, p_2, \ldots, p_n\} \equiv p$. In our quantum-mechanics modeling, we write $\hat{H} = \hat{H}(p)$ and address the solution taking the form of an eigenvalue problem $\hat{H}\psi_\nu = e_\nu \psi_\nu$. In the jargon of applied mathematics, one expresses the same by saying that $\hat{\mathcal{M}}$ acts upon the set of optimized parameters p^{opt}, providing results $e \leftrightarrow \{e_\nu\}$, or, that one is solving a *direct problem*:

$$\hat{\mathcal{M}}\, p^{\text{opt}} = e, \tag{14}$$

under the condition that the optimal parameters of the model are known. If the optimal parameters are not yet known, they are obtained by solving the *inverse problem*

$$\hat{\mathcal{M}}^{-1}\, e = p^{\text{opt}}, \tag{15}$$

under the condition that the inverse, $\hat{\mathcal{M}}^{-1}$, exists; otherwise, we say that the *inverse problem is ill posed*. Construction of $\hat{H}^{-1} \leftrightarrow \hat{\mathcal{M}}^{-1}$ in realistic cases, even for nuclear mean-field theory Hamiltonians considered relatively simple, does not exist and the issue of the formal ill posedness and its possible practical implications remains open.

Whereas the notion and properties of $\hat{\mathcal{M}}^{-1}$ are fundamental in formalizing the issue of instabilities of a model in applied mathematics, the present-case parameter optimization is accomplished via χ^2 minimization ignoring a possible *formal* ill posedness of the inverse problem. It turns out that overparametrized models, i.e., the ones in which parameter optimization leads to solutions with certain parameters being functions of some others, lead to ill posedness of modeling and destabilization of the prediction capacities both in the case of the formal solving of the inverse problem as well as the χ^2 minimization.

The issues of overparameterization can be treated relatively straightforwardly with the help of the so-called *singular value decomposition* theorem, which allows us to detect and quantify the model prediction instabilities (cf., e.g., Sec. 5 of Ref. [37] for illustrations very close to the present context, yet manifesting certain shortcomings discussed there). Alternatively, parametric correlations one can be detected and consecutively eliminated with the help of Monte Carlo

techniques. There exists a number of published illustrations of such approaches, which we refer to as pilot projects. They discuss parametric-correlation detection and implied prediction instabilities in a series of simplified illustrations using nuclear mean-field theoretical methods very close to ours and are briefly overviewed in the following section.

C. Earlier pilot projects addressing parametric correlation problem: An overview

We believe that it will be instructive to present for comparison a short overview of the pilot projects mentioned before addressing our results. In particular, Refs. [35,36] illustrate the effects of varying numbers of experimental data points on the adjustment of parameters using as an illustration the neutron experimental levels of ^{208}Pb. The authors detect the presence of parametric correlations within the Hamiltonian tested while comparing the correlation-matrix and Monte Carlo techniques, but the discussion is limited to a single nucleus. Tests in a similar style are discussed in Ref. [37], where the single-nucleus type adjustments for ^{208}Pb are employed to test predictive power for the levels in the neighboring doubly magic nucleus ^{132}Sn. Singular-value decomposition theorem is discussed in the context of the parametric correlation analysis as an alternative to the Monte Carlo approach and a number of open problems are indicated.

A physics argument (rather than that employing applied mathematics techniques alone) leading to a decrease in the number of the model parameters—at a comparable quality performance—has been discussed and illustrated in Ref. [38] in the case of the Woods-Saxon mean-field Hamiltonian. The authors at the same time decrease the number of the spin-orbit potential parameters replacing the traditional form by more microscopic density-dependent analogs; cf. Eqs. (20)–(22) of the above reference.

Discussion of alternative methods possibly leading to an increase of the modeling stability is presented in Ref. [39] by employing a powerful technique of exact modeling. The latter uses known solutions of realistic Hamiltonians in order to study the structures of parametric correlations and single-nucleon energy sensibility to various parameters.

As it turns out, the issue of the parametric correlations more strongly impacts the microscopic realizations of the nuclear mean field theory such as Hartree-Fock and/or Hartree-Fock-Bogolyubov, compared to more phenomenological Woods-Saxon type realizations. These issues are addressed in Ref. [40] using correlation-matrix and singular-value decomposition techniques. The reader may also consult Sec. 6 of the above article referring to certain general publications related to inverse problem as related to physics applications of interest in our case.

Monte Carlo parameter adjustment techniques provide relatively direct manners of detecting mathematical forms of the parametric correlations. In Ref. [41], the authors address systematically correlations among all Woods-Saxon potential parameters. They find in particular that the diffusivity parameters do not correlate either with the radius or the depth (strength in the case of the spin-orbit term). At the same time, the potential radius and depth (strength) parameters form approximately parabolic functional dependencies. They were determined for the ^{208}Pb case and their impact on the uncertainty probability distributions for single-nucleon levels.

Considerations introduced in Ref. [38] are developed further in Ref. [42], addressing in detail the nucleonic-density-dependent spin-orbit potential parametric correlations showing that the parametric freedom of the original phenomenological formulations, where spin orbit depends on six parameters, is reduced to a single independent one.

In the present article, in contrast to the pilot-project studies just cited, the mean-field model parameters are adjusted for the first time to eight doubly magic spherical nuclei listed in Eq. (16) using Monte Carlo methods, and the parametric correlations are systematically studied, detected, and eliminated. We believe that by selecting this approach, which follows the recommendations of the inverse problem theory of applied mathematics, we increase stabilization of predictions obtained in this article.

III. PARAMETER OPTIMIZATION

The mean-field Hamiltonian parameters are adjusted using the χ^2 test to the experimental values of single-nucleon level energies in doubly magic spherical nuclei

$$^{16}\mathrm{O},\ ^{40}\mathrm{Ca},\ ^{48}\mathrm{Ca},\ ^{56}\mathrm{Ni},\ ^{90}\mathrm{Zr},\ ^{132}\mathrm{Sn},\ ^{146}\mathrm{Gd},\ ^{208}\mathrm{Pb}; \quad (16)$$

the corresponding energies were extracted in Ref. [37]. In the case of adjusting Hamiltonian parameters to the data of more than one nucleus (eight nuclei simultaneously in the present case), it is customary to introduce explicitly the isospin dependence in the strength parameters of central and spin-orbit potentials in the forms

$$V^{\mathrm{c}}_{\pi,\nu} = V^{\mathrm{c}}_0\left(1 \pm \kappa^{\mathrm{c}}\frac{N-Z}{N+Z}\right) \quad (17)$$

and

$$\lambda^{\mathrm{so}}_{\pi,\nu} = \lambda^{\mathrm{so}}_0\left(1 \pm \kappa^{\mathrm{so}}\frac{N-Z}{N+Z}\right), \quad (18)$$

correspondingly, with the plus sign for the protons and the minus sign for the neutrons. Above, V^{c}_0, λ^{so}_0, and κ^{c} and κ^{so} are new adjustable constants, so that symbols

$$\left\{V^{\mathrm{c}}_0, \kappa^{\mathrm{c}}; \lambda^{\mathrm{so}}_0, \kappa^{\mathrm{so}}\right\} \quad \leftrightarrow \quad \left\{V^{\mathrm{c}}_\pi, V^{\mathrm{c}}_\nu; \lambda^{\mathrm{so}}_\pi, \lambda^{\mathrm{so}}_\nu\right\} \quad (19)$$

appear interchangeably with the symbols introduced in Eq. (6), but the new parameter set is better adapted when adjusting parameters for several nuclei simultaneously thanks to the built-in specific Z and N dependence.

A. Comments about definition of $\chi^2(p)$ function

The parameter set p used in the present article has been obtained by minimizing the distance between the sets of experimental $\{e^{\mathrm{exp}}_i\}$ and model energies $\{e^{\mathrm{th}}_i\}$. This distance is defined as usual by

$$\chi^2(p) = \sum_{i=1}^{n_d} w_i\left[e^{\mathrm{exp}}_i - e^{\mathrm{th}}_i(p)\right]^2. \quad (20)$$

The summation limit in Eq. (20) represents the total number of experimental data points, the energy levels in all eight nuclei listed in Eq. (16). The adjustable parameters are denoted by p. According to the usual rules of application of the χ^2-minimization techniques, definition of the ensemble of the weight factors $\{w_i\}$ is left to a subjective judgment of the constructor of the model. Since we are using the experimental data on spherical nuclei, each of the single-particle levels can be characterized, among others, by the angular-momentum quantum number $j \to j_i$ so that our natural choice of the weight factors, taking into the account spherical degeneracy, is

$$w_i = (2j_i + 1). \tag{21}$$

Summation in the χ^2 definition, Eq. (20), accounts for all the nuclei of interest at the same time. It then follows that according to Eqs. (20) and (21), certain nuclei can be overrepresented as compared to the others. For instance, the highest j value in ^{16}O is $j = 5/2$, whereas the highest one in ^{208}Pb is $j = 13/2$ with the result that the χ^2 definition as it stands privileges heavy nuclei. This, however, is not necessarily desirable for the optimal functioning of the model since the concept of universal parametrization involves implicitly two requirements:

(1) The mean-field parameters are fixed once for all the nuclei in the mass table and
(2) the quality of the description of single-nucleon properties should be comparably satisfactory without (de)privileging certain subensembles of nuclei.

To enable a certain control of the above concept of universality, we introduce extra weight factors, $\tilde{w}_k$, for $k = 1, 2, \ldots, 8$; cf. Eq. (16). We define them as dependent on the mass numbers A_k of intervening nuclei relative to the mass number of ^{208}Pb treated as reference:

$$\tilde{w}_k = 208/A_k. \tag{22}$$

Thus, the final expression for $\chi^2(p)$ takes a new form:

$$\chi^2(p) = \frac{\sum_{k=1}^{\mathcal{N}} \tilde{w}_k \sum_{i=1}^{n_k} \left\{(2j_{i,k}+1)\left[e_{i,k}^{\rm exp} - e_{i,k}^{\rm th}(p)\right]^2\right\}}{\sum_{k=1}^{\mathcal{N}} \tilde{w}_k}. \tag{23}$$

Within this new notation, $\mathcal{N} = 8$ is the number of all nuclei considered in the experimental sampling and n_k are the numbers of available experimental energy levels in each nucleus k, whereas $e_{i,k}^{\rm exp}$ and $e_{i,k}^{\rm th}(p)$ are, respectively, the experimental and theoretical single nucleon energy levels with $i = 1, 2, \ldots, n_k$ for $k = 1, 2, \ldots, \mathcal{N}$. With the single-particle energies $e_{i,k}^{\rm th}(p)$ obtained as solutions of the Schrödinger equation with the Hamiltonian of Eq. (1), the resulting $\chi^2(p)$ has been minimized. In the present article, we employ the standard Levenberg-Marquardt minimization algorithm.

B. Monte Carlo simulations: Selected issues

Our analysis of parameter adjustment and of the parametric correlations takes into account the experimental error bars. This is straightforward via application of the Monte Carlo techniques which provide information in the form of probability distributions rather than fixed numerical values of optimal parameters. In calculations of the nuclear-potential energy surfaces, the most probable values of the Hamiltonian parameters have been used.

To describe briefly the applied Monte Carlo treatment, it will be convenient to employ a simplified notation often used in this context. For this purpose, we express the experimental energies, previously denoted $\{e_{i,k}^{\rm exp}\}$, with the help of one-index notation as

$$\left\{e_{i,k}^{\rm exp}\right\} \;\to\; \left\{d_1, d_2, d_3, ..., d_{n_d}\right\} \tag{24}$$

with d for datum, and the uncertainties resulting from experimental error bars by corresponding Gaussian widths

$$\left\{\sigma_1, \sigma_2, \sigma_3, ..., \sigma_{n_d}\right\}. \tag{25}$$

In analogy, let the sequence of parameters originally introduced in Eq. (6) be redefined as

$$\left\{p_1, p_2, p_3, ..., p_{n_p}\right\}, \tag{26}$$

where $n_p = 12$; cf. Eq. (6) and compare with Eq. (19). We introduce the Gaussian noise distributions $\mathcal{N}(d_i, \sigma_i)$, also called "normal," with centers d_i and widths σ_i.

We are interested in discovering the possible presence of correlations between parameters, say, p_i and p_j, treated as random variables. For this purpose—as a convenient auxiliary step on top of the Monte Carlo simulations—we will use the correlation matrix (Pearson coefficients). For the reader's convenience, we recall its definition. Again, avoiding multi-index notation and without loosing generality, let us consider explicitly two random variables only, say x and y. With the associated random sampling which involves $\alpha = 1, 2, \ldots, n$ repetitions, one defines Pearson coefficient as

$$\mathcal{P}_{x,y} \equiv \frac{\sum_{\alpha=1}^{n}(x_\alpha - \bar{x})(y_\alpha - \bar{y})}{\sqrt{\sum_{\alpha=1}^{n}(x_\alpha - \bar{x})^2 \sum_{\alpha=1}^{n}(y_\alpha - \bar{y})^2}}, \tag{27}$$

where $\bar{x}$ and $\bar{y}$ denote the corresponding sample means. This definition can be applied to any combination of parameters, e.g., $x \leftrightarrow p_i$ and $y \leftrightarrow p_j$, leading more generally to diagonal and nondiagonal combinations such as $\mathcal{P}_{p_i,p_i}$, $\mathcal{P}_{p_j,p_j}$, $\mathcal{P}_{p_i,p_j}$, e.g., $\mathcal{P}_{r_\pi^c,V_0^c}$. The numerical values of these coefficients lie in the interval $[-1, +1]$. In particular, the nondiagonal values of the Pearson coefficient close to 0 (or vanishing), e.g., $\mathcal{P}_{a_\pi^c,V_0^c} \approx 0$, would signify that the central-potential proton diffuseness and the depth parameters are uncorrelated, whereas $\mathcal{P}_{r_\pi^c,V_0^c} \approx \pm 1$ would imply strong linear correlations between the two.

In the present Monte Carlo simulations, we generate numerically $N_{\rm MC} \approx 10^5$ times the $N_{\rm MC}$ n_d-tuples of the input data sets according to $\mathcal{N}(d_i, \sigma_i)$ for $i = 1, 2, \ldots, n_d$. We perform each time the χ^2 minimization and define in this way the $N_{\rm MC}$ n_p-tuples of parameters. It is then convenient to illustrate the so-obtained results in the form of projection diagrams shown in Figs. 1 and 2, which represent graphically the number of occurrences for each parametric solution as the result of the χ^2 minimization. This representation is more indicative compared to Pearson coefficient approach since it provides explicitly a functional dependence not limited to linear correlations.

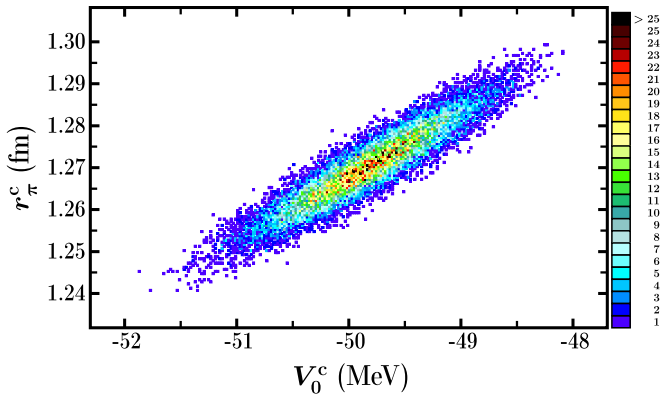

FIG. 1. Parametric correlations between the central potential radius and depth parameters for protons suggestive of approximately linear dependence. Pearson coefficient is very close to 1, confirming strong correlations; for details, see the text. For this illustration, we arbitrarily select a color scale composed of 25 colors.

Results for protons projected on the plane (r_π^c, V_0^c) in Fig. 1 show clearly an approximately linear correlation between these two parameters. Results for the neutrons are very similar and are not shown. The corresponding Pearson coefficient is close to unity, confirming independently the strong correlation between these parameters. Analogous analysis reveals that there are no correlations between V_0^c and $a_{\pi,\nu}^c$ and thus between $r_{\pi,\nu}^c$ and $a_{\pi,\nu}^c$, nor correlations involving κ^c, all with Pearson coefficients close to 0. We conclude that among the six parameters of the central Woods-Saxon potential originally treated as independent, there are two two-parameter correlations, one pair for the protons and one for the neutrons. Thus, without loosing generality, we select as independent V_0^c, κ^c, a_π^c, and a_ν^c, which are then effectively optimized.

The spin-orbit potential manifests strength versus radius ($r_{\pi,\nu}^{so}$ versus λ_0^{so}) parametric correlations as well. They reveal a characteristic form shown in Fig. 2 for protons: double valued rather than a single functional relation. The possibility of revealing multivalued dependencies is a significant advantage of the Monte Carlo techniques over the single-point Pearson

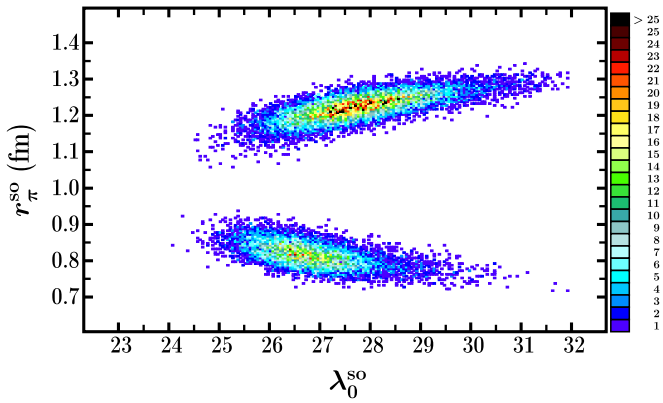

FIG. 2. Parametric correlations for the spin-orbit potential reveal two approximately linear dependencies as discussed in the text; observe the double-valued functional relation.

TABLE I. Woods-Saxon parameter values adopted in this project. Upper row: proton parameters; lower row: neutron parameters. The dependent parameters resulting from the linear dependencies discussed and corresponding to V_0^c and λ_0^{so}: $r_\pi^c = 1.278$ fm, $r_\nu^c = 1.265$ fm, $r_\pi^{so} = 0.830$ fm, $r_\nu^{so} = 0.890$ fm. For the choice of diffusivities, $a_\pi^{so} = a_\nu^{so} = 0.700$ fm; see text.

	V_0^c (MeV)	κ^c	$a_{\pi,\nu}^c$ (fm)	λ_0^{so}	κ^{so}
Mean values	−50.225	0.624	0.594 0.572	26.210	−0.683
Standard error	0.142	0.013	0.010 0.011	0.513	0.139

correlation test. The results for the neutrons are similar and are not shown.

The peculiarity in the form of the double-valued dependence of the radius parameter $r_{\pi,\nu}^{so}$ as function of λ_0^{so} brings us to the conclusion that the Woods-Saxon spin-orbit Hamiltonian leads to two variants of parametrizations differing from one another in terms of the two characteristic spin-orbit radii: a smaller parameter value, $r_{\pi,\nu}^{so} < 1$ fm, referred to as *compact*, and the larger one, $r_{\pi,\nu}^{so} > 1$ fm, referred to as *noncompact*.

This type of behavior is not unusual when working with strongly nonlinear modeling like in our case. Generally, nonlinear modeling may lead to more than just one minimum of the χ^2-test function and this is up to the constructor of the model to decide which of the competing minima (the global or a local one) should be privileged. For instance, in the nuclear structure mean-field parameter adjustment, we may attribute high priority to reproducing the experimental level *ordering*, the condition which may not accord with the simultaneous absolute minimum in terms of the χ^2. Therefore, depending on the context, in the presence of the multiple minima of the χ^2 function we may formulate arguments for not selecting the absolute one. In this article, we have selected the compact solution since it has been verified that—at comparable quality of the correspondence between theoretical and experimental single-nucleon energies—such a choice leads on average to slightly better description of the rotational properties of many nuclei.

Relations like the ones illustrated in Figs. 1 and 2 allow us to chose one of the two parameters for playing the role of the independent variable. By doing so, we were able to reduce the number of independent parameters from originally 12 to 8. These are $\{V_0^c, \kappa^c\}$ as well as a_π^c and a_ν^c for the central potential and $\{\lambda_0^{so}, \kappa^{so}\}$ as well as a_π^{so} and a_ν^{so} for the spin-orbit one. Since the spin-orbit diffuseness parameter influences the single-nucleon spectra in a very regular and/or smooth manner, in this project we have set a_π^{so} and a_ν^{so} equal to 0.7 fm, the value adapted long ago within the traditional universal Woods-Saxon parametrization of Ref. [16].

Table I summarizes the values adopted in this project.

In the rest of this article, we will focus the discussion on the mean-field predictions of the shape coexistence in the light-mass range of the nuclear mass table with the proton number Z varying between 14 and 46 charge units.

Illustrations which will be presented were selected from the full set of total energy calculations including over 240 even-even nuclei for which experimental-existence indications can be found in the National Nuclear Data Center (NNDC) database as well as for a number of very exotic proton-rich and neutron-rich nuclei.

IV. PARAMETRIC UNCERTAINTIES: IMPACT ON CALCULATED NUCLEAR ENERGIES

We discussed the forms of parametric correlations which result from the Hamiltonian optimization in Sec. III B, Figs. 1 and 2. They are very characteristic in the case of the Woods-Saxon phenomenological mean-field Hamiltonian. In particular, diffusivity parameters both for the central potential, $a^{c}_{\pi,\nu}$, and for the spin-orbit potential, $a^{so}_{\pi,\nu}$, do not couple with the other parameters via parameter optimization process. In contrast, the central radius and central potential-strength parameters, r^{c} and V^{c}_{0} and independently r^{so} and λ^{so}_{0}, do couple, forming approximately linear relations of the form

$$r^{c} = f^{c}\left(V^{c}_{0}\right) \quad \text{and} \quad r^{so} = f^{so}\left(\lambda^{so}_{0}\right), \tag{28}$$

for the protons and for the neutrons, independent from one another.

Since Monte Carlo simulations allow determining the above relations beforehand, i.e., within the original space of 12 parameters, six for the protons and six for the neutrons, the four relations in Eq. (28) were predetermined before proceeding to optimize the eight free parameters remaining after the correlation removal. This step leads via eight-parameter Monte Carlo simulation not only to the optimal values of parameters, i.e., eight numbers but, importantly, to the probability distributions in eight-dimensional space resembling eight-dimensional Gaussian distributions. The latter allow obtaining the new set of projected one-dimensional distributions for each parameter of interest.

We will present distributions like the one in Fig. 3 for selected parameters of interest, assuming that all the remaining seven parameters take their maximum probability values. These distributions closely resemble Gaussian forms. They were constructed producing the relevant histograms and fitting the Gaussian dependencies whose parameters will be displayed in the figures which follow. Figure 3 represents the Gaussian uncertainty probability distribution for the central potential depth parameter.

There is no unique way of illustrating the effects of the uncertainties of the parameters of the nuclear mean-field Hamiltonian, which are represented by continuous probability distributions. Expression of the total nuclear energy, which is the main interest in the present test, involves among others macroscopic energy, the latter independent of the mean-field Hamiltonian. Therefore, we propose illustrating the variation of the Strutinsky shell energy with the Hamiltonian parameters as a measure of parametric sensitivity in the context of total energy calculations. Illustrations shown below display the differences between shell energies obtained with the potential depth parameter corresponding to the mean value of V^{c}_{0} and the value increased by the amount of FWHM (full width at half maximum); these numerical values are explicitly displayed in the field of Fig. 4.

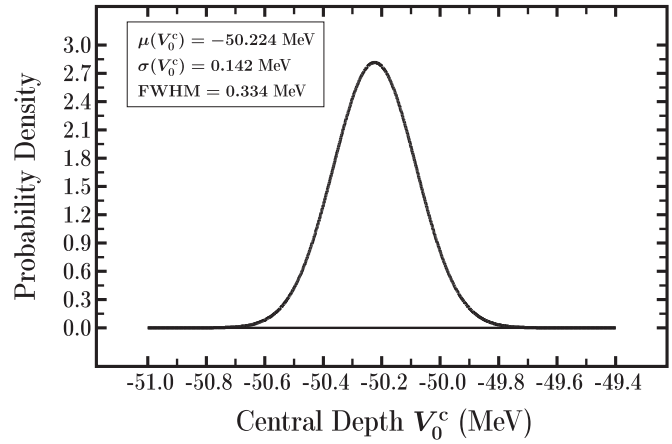

FIG. 3. Uncertainty probability distribution for the central potential depth parameter V^{c}_{0}. Fitting for eight nuclei listed in Eq. (16) involves 45 experimental data points for the protons and 60 data points for the neutrons. The values of Gaussian mean μ and standard deviation σ are given in the figure together with the full width at half maximum relative to the mean, denoted FWHM.

Since we explore rather extreme variations of nuclear deformations in the present article, investigating the evolution of the discussed uncertainties as functions of nuclear shape is of clear interest. Results in Fig. 4 indicate the presence of fluctuations (rather than systematic increase) which limit the impact of uncertainties and whose variations do not exceed ±50 keV interval.

As a final comment at this point, let us remark that within the Strutinsky approach, the shell and the paring correction (correlation) energy contributions appear very often with

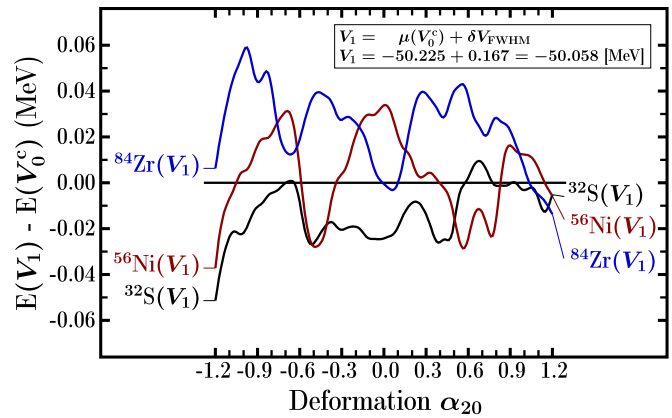

FIG. 4. Variation of Strutinsky shell energy for the nuclei displayed. They are represented as the differences between the values corresponding to the potential depth equal V^{c}_{0}, the curve treated as normalization, and the same quantity calculated at the shift by the value corresponding to the FWHM value from Fig. 3, shortened to V_1. The deviations are interpreted as measures of uncertainties of the final results; they vary within energy stripe defined by ±50 keV limits.

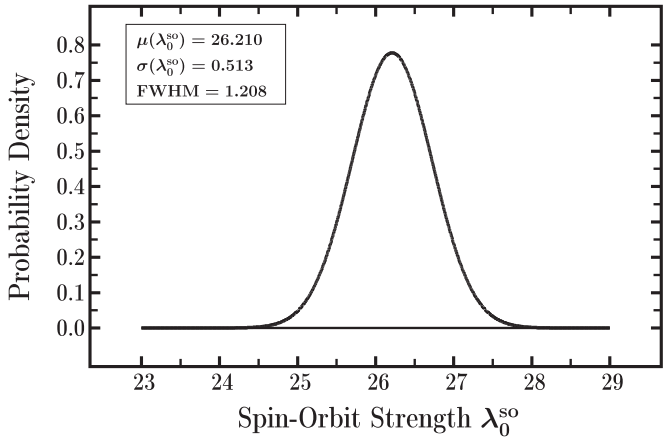

FIG. 5. Uncertainty probability distribution for the spin-orbit strength parameter λ_0^{so}; for details cf. caption to analogous illustration in Fig. 3.

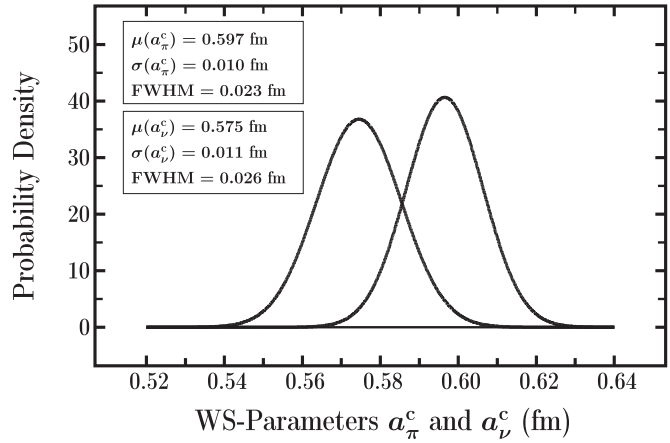

FIG. 7. Uncertainty probability distributions for diffusivity parameters for the Woods-Saxon potential for protons and neutrons.

opposite signs. This indicates that the uncertainties illustrated above can be seen as upper limits and are very likely representative for the actual uncertainty variations.

The uncertainty distribution for the spin-orbit strength parameter λ_0^{so}, analogous to the one in Fig. 3, is given in Fig. 5. The impact of those uncertainties for the Strutinsky shell-energy dependence on quadrupole deformation is shown in Fig. 6.

We finish by presenting analogous uncertainty effects implied by the uncertainties of the central-potential diffusivity parameters, cf. Fig. 7, and the implied impact on the calculated total potential energies, Fig. 8.

As expected, parametric uncertainties induce much stronger effects on the calculated nuclear energies in the case of the spin-orbit potential strength. Indeed, whereas the single-nucleon energies vary with the central potential depth in a very regular fashion, the spin-orbit term which controls relative positions of various orbitals has a direct impact on the shell gaps, the latter influencing directly the shell energies. It is fair to say that the obtained uncertainties vary within an interval approximately a factor of 10 larger as compared to the central-potential case. The strongest effects are seen at the spherical shapes where the shell effects are usually significant and vary relatively strongly with nucleon numbers.

V. FROM ADJUSTMENTS AT SPHERICAL SYMMETRY TO DEFORMATION EFFECTS

In the preceding sections, we have given the arguments that the parameter optimization technique chosen should give stable predictions when moving with the Z and N numbers away from the fitting zone of the mass table. On the other hand, before engaging in predictions of possibly new exotic geometrical symmetries and/or extreme deformations, it is natural to verify whether the correctly described spherical-shell properties propagate equally satisfactorily into the (Z, N) areas of nuclei which are deformed in their ground states.

The deformation dependence of single-particle energies obtained with the parameters optimized in this article is shown in Fig. 9 and it is important to test the implied ground-state equilibrium deformations versus experiment. Many data exist

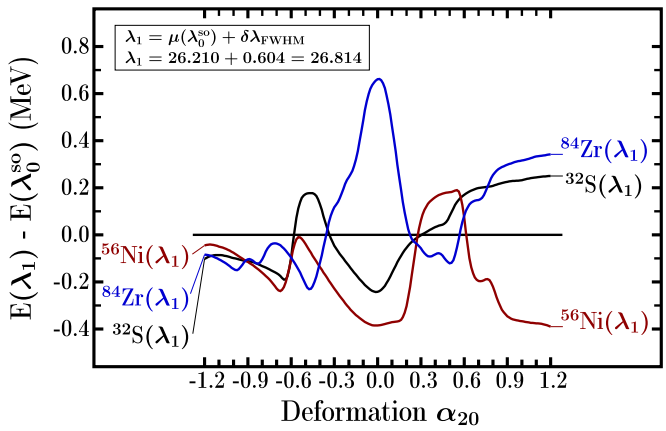

FIG. 6. Variation of the shell-energy for nuclei displayed; cf. caption to Fig. 4. The maximum at $\alpha_{20} \approx 0$ for ^{84}Zr nucleus reflects the presence of the strong gaps at $Z = N = 40$.

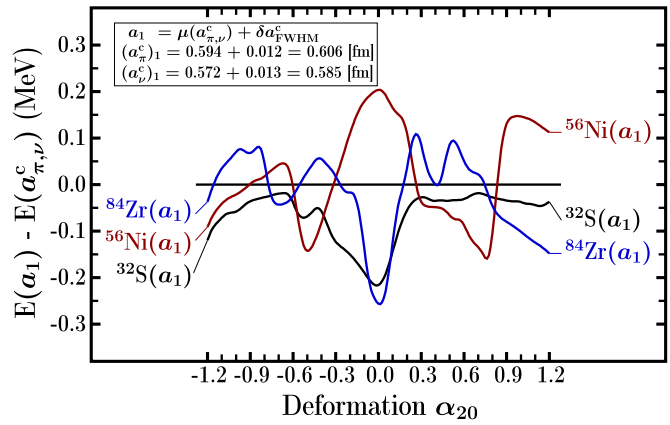

FIG. 8. Illustration analogous to the ones in Figs. 4 and 6 but for the diffusivity parameters for protons and neutrons, here tested at the same time.

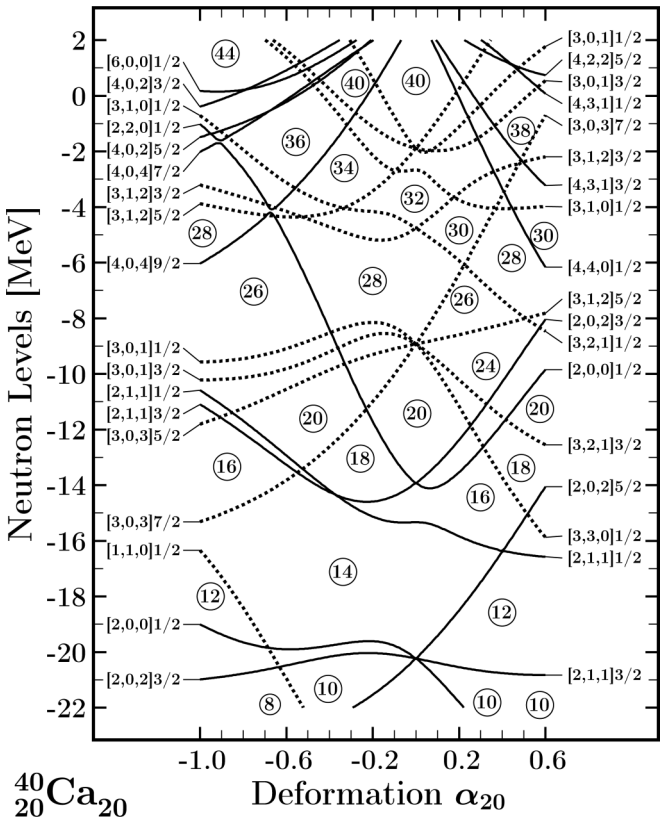

FIG. 9. Neutron single-particle energies as functions of the quadrupole deformation α_{20}, focusing on the negative α_{20} portion (oblate shapes) of the quadrupole deformation axis. Full (dotted) lines refer to positive (negative) parity. Analogous diagram for protons is nearly identical and is not shown.

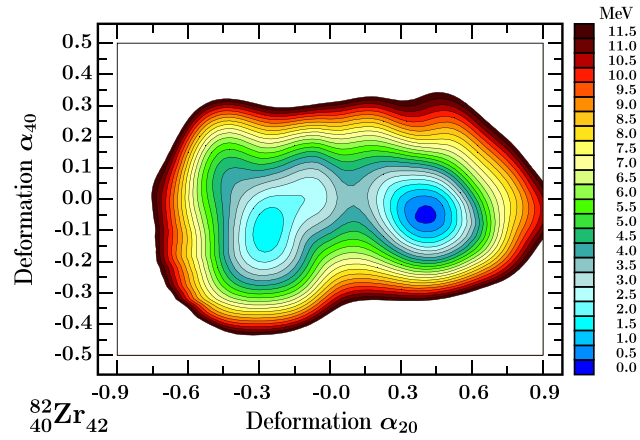

FIG. 10. Nuclear potential energy for ^{82}Zr projected on the quadrupole/hexadecapole plane of variables α_{20} and α_{40}. The ground-state minimum predicted at $\alpha_{20}^{\rm th} = 0.38$ remains in excellent agreement with the experimental rms estimate of $\alpha_{20}^{\rm exp} = 0.368(^{+24}_{-10})$ from Ref. [44].

today; cf., e.g., Refs. [43–45]. Therefore we first compare the results for equilibrium deformations for specifically chosen nuclei before passing to the discussion of exotic symmetries or exotic-shape predictions, the central focus of this article.

Let us emphasize that nuclear deformations, and in particular the quadrupole ones, which are used below to relate to experiment, are *not* observables and that the corresponding experimental information can only be extracted indirectly. The usual procedure consists in transforming the measured nuclear lifetimes into reduced transition probabilities, the latter depending on the quadrupole moments, which in turn can be expressed by nuclear shape parameters—all this while employing a number of approximate steps. As the result, the implied comparison theory-experiment should not be treated as a strict one-to-one bijection. This being said, compilations in Refs. [43,44] provide rich collection of *rms average* quadrupole deformations $\langle\beta_2^2\rangle_{\rm rms} \leftrightarrow \langle\alpha_{20}^2\rangle_{\rm rms}$, with a disadvantage that the sign of quadrupole deformation parameters is not determined. In contrast, Ref. [45] provides the distinction between the prolate and oblate configurations but for a significantly smaller number of nuclei.

As is well known, the spherical geometry in relatively light nuclei considered in this article is usually associated with the combination of the proton-neutron spherical shell closures at $Z_{\rm sph}, N_{\rm sph} = 40, 28, 20$ down to 14; cf. Fig. 9 and compare with Ref. [13]. Varying the Z and/or N numbers around the above spherical shell closures, we find several transitional nuclei with flat potential energy surfaces and no clearcut indication of any preference for the well-defined equilibrium deformation. Such cases are not well suited even for semiquantitative comparison of the equilibrium deformations with the experimental ones, which we would like to obtain at present. However, by varying the nucleon numbers still further, one often obtains clearer indication of well-pronounced equilibrium shape minima with the well-defined separating barriers. Such nuclei will be chosen for quality test of prediction capacities for nonspherical nuclei.

We begin by comparison for selected $Z = 40$ isotopes. The predicted shape properties of the lightest zirconium isotope for which we find the experimental information about the equilibrium deformation, ^{82}Zr, are illustrated in Fig. 10, projection from $\{\alpha_{20}, \alpha_{30}, \alpha_{40}\}$ space. The measured average equilibrium deformation is $\alpha_{20}^{\rm exp} = 0.368(^{+24}_{-10})$ according to Ref. [44]. It should be compared with $\alpha_{20}^{\rm th} = 0.38$; the two can be considered as nearly coinciding, encouraging further tests.

The neighboring ^{84}Zr has the experimental rms average α_{20} equilibrium significantly (by 38%) lower. Indeed, the experimental average rms result from Ref. [44] is $\alpha_{20}^{\rm exp} = 0.251(^{+72}_{-63})$ as compared to the calculation result, here in the form of a pronounced oblate/prolate shape coexistence with either $\alpha_{20}^{\rm th} = -0.28$ or $\alpha_{20}^{\rm th} = +0.31$; cf. Fig. 11. Given the fact that the sign of the experimental deformation parameter is undermined, comparison can be interpreted as satisfactory.

Note that the compared values in ^{84}Zr are lower by about 38% *in both theory and experiment* as compared to the neighboring ^{82}Zr; again the result which can be seen as strongly encouraging.

Experimental results for the ground-state equilibrium deformations for still larger neutron numbers, i.e., for ^{86}Zr up to ^{98}Zr are characterized by significantly lower values $\alpha_{20}^{\rm exp}$, varying typically between 0.1 and 0.05. This can be seen as the reflection of the closeness to $N = 50$ spherical shell closure.

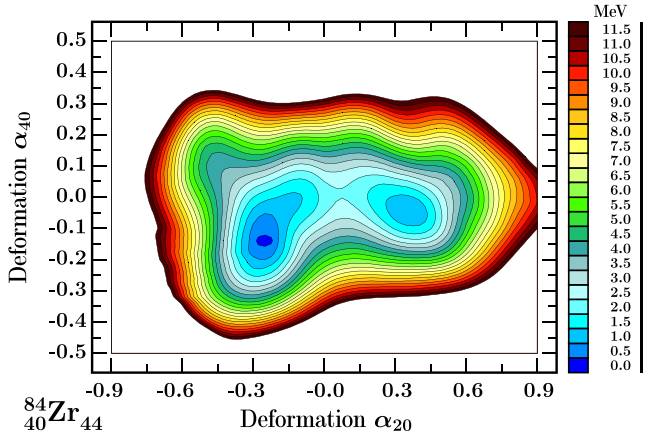

FIG. 11. Similar to the preceding one for ^{84}Zr. Experimental average equilibrium $\alpha_{20}^{\rm exp} = 0.251(^{+72}_{-63})$, after Ref. [44], compares quite well up to the sign with either $\alpha_{20}^{\rm th} \approx 0.32$ or $\alpha_{20}^{\rm th} \approx -0.29$; see the text for further comments.

Since theoretical results are fully coherent with this behavior, they are not shown here.

Instead, we wish to verify the correspondence of theory and experiment at the upper limit of this chain which is characterized by a significant jump from $\alpha_{20}^{\rm exp} \approx 0.03$ for ^{98}Zr to $\alpha_{20}^{\rm exp} = 0.356(^{+82}_{-57})$ for ^{100}Zr (cf. Refs. [43,44]). The corresponding theory results are, respectively, $\alpha_{20}^{\rm th} \approx 0$ and $\alpha_{20}^{\rm th} = 0.32$; cf. Fig. 12 illustrating the ^{100}Zr case. This, in our opinion, can be considered again as a strong confirmation of the modeling shape-prediction capacities.

It is neither the place here nor our intention to discuss case after case the evolution of the shape properties for over a couple of hundred even-even nuclei in the sector of the mass table selected for this article. Instead we would rather like to select a few nonoverlapping zones on the (Z, N) plane and complete our comparison addressing the nuclear combinations with

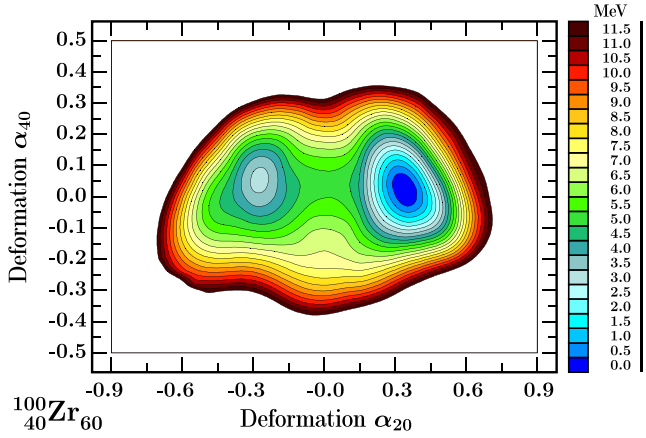

FIG. 12. Similar to the preceding ones but for ^{100}Zr. The experimental result for the average quadrupole deformation, $\alpha_{20}^{\rm exp} = 0.356(^{+82}_{-57})$, compares very well with $\alpha_{20}^{\rm th} \approx 0.32$ as seen from the plot. Together with the characteristic jump from nearly zero deformation in ^{98}Zr to over 0.30 in ^{100}Zr, the comparison gives strong support for the prediction capacities of the model parametrization.

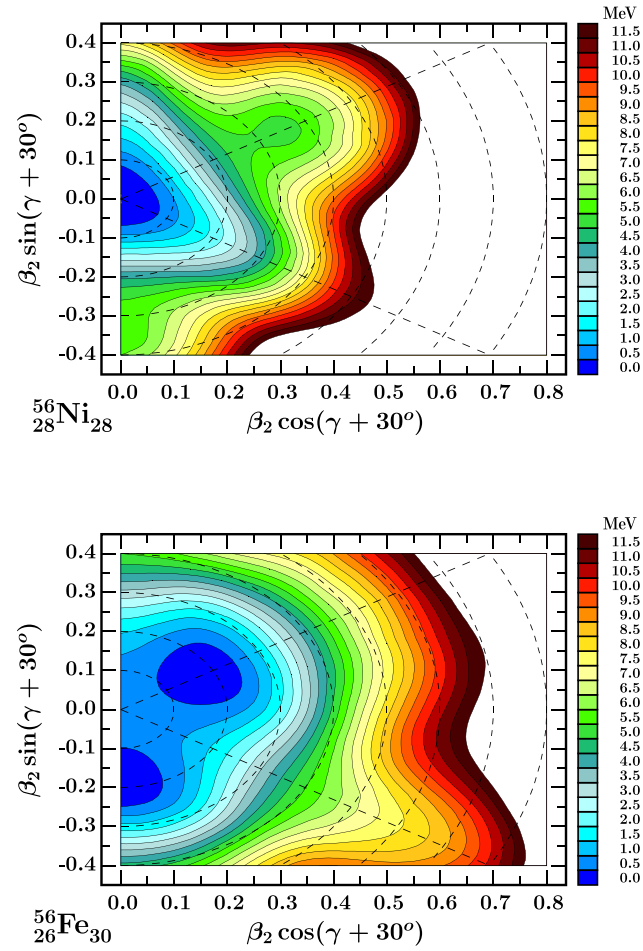

FIG. 13. Total energy projections on the standard (β, γ) plane of quadrupole axial and triaxial deformations for ^{56}Ni (top) and ^{56}Fe (bottom) as discussed in the text. At each point, a minimization over α_{40} has been performed. Whereas the doubly magic ^{56}Ni is predicted spherical, the ^{56}Fe is predicted nonspherical with the axial quadrupole deformation in good agreement with the experimental value; see text.

strong jumps in terms of the equilibrium deformations from a given nucleus to its near neighbor. We believe that this type of a comparison offers possibly the most convincing arguments in favor of (or against) the predictive power of modeling.

In this context, it will be instructive to compare the properties of the doubly magic $Z = 28$ and $N = 28$ nucleus ^{56}Ni appearing in our calculations as expected as spherical (cf. Fig. 13, top) and its nearest neighbors, some of which are known from experiment to be deformed. Such known deformed neighboring nuclei involve combinations of $Z = 26$, 30 and $N = 26$, 30.

We continue with $^{56}_{26}Fe_{30}$, whose potential energy is illustrated in Fig. 13, bottom. Indeed the experimental equilibrium deformation for ^{56}Fe, after Ref. [44], is $\alpha_{20}^{\rm exp} = 0.239(2)$ which should be compared with the calculated value $\alpha_{20}^{\rm th} \approx 0.19$ seen from the figure, in a good semiquantitative correspondence given the flatness of the potential energy surface. Unfortunately, continuation either with $^{56}_{30}Zn_{26}$ or with $^{60}_{30}Zn_{30}$

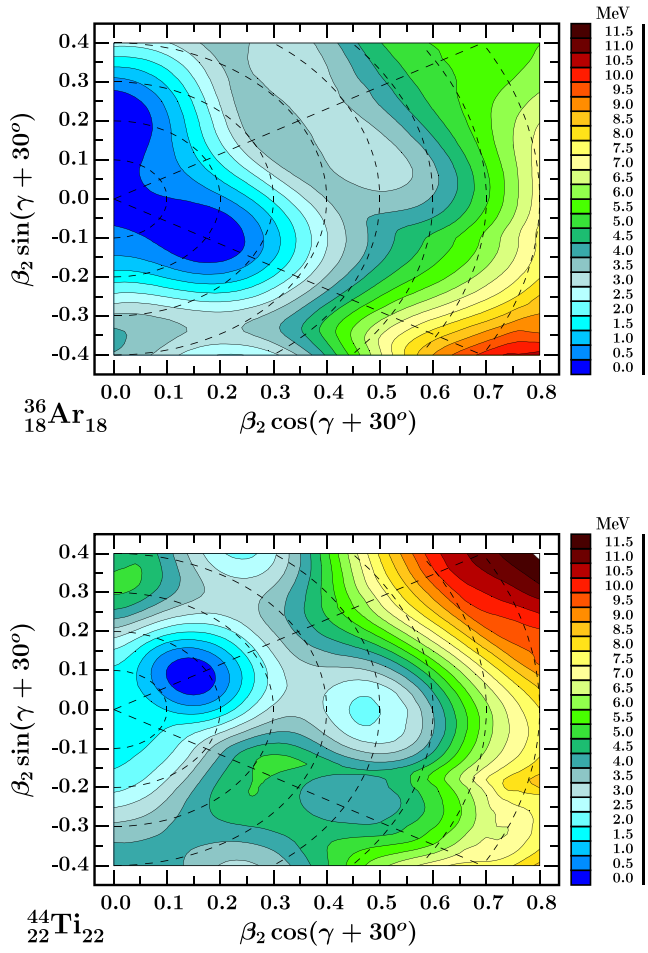

FIG. 14. Similar to the preceding one but for ^{36}Ar (top), showing two valleys extending toward oblate-shape directions in the (β, γ) plane with deformations of $\gamma = \pm 60^\circ$ and ^{44}Ti (bottom) as discussed in the text. In the latter case, the prediction of the superdeformed triaxial secondary minimum deserves noticing.

turns out not to be possible because of the missing experimental information. Instead, the results for $^{52}_{26}\mathrm{Fe}_{26}$ are available. We find the experimental value $\alpha_{20}^{\mathrm{exp}} = 0.230(14)$ compared with $\alpha_{20}^{\mathrm{th}} \approx 0.22$, a perfect correspondence.

To continue illustrations of prediction capacities of our modeling with its universal parametrization, we focus here on the nearest neighbors of the next doubly magic spherical shell closure, $Z = 20$ and $N = 20$, ^{40}Ca. We wish to profit from the fact that for $Z = 18$ and $N = 18$ as well as $Z = 22$ and $N = 22$, i.e., ^{36}Ar and ^{44}Ti nuclei, cf. Fig. 14, both experimental equilibrium deformations are known and are significantly different from zero. The total energy map for the doubly magic ^{40}Ca indicates spherical equilibrium; the corresponding plot resembles the one for ^{56}Ni, Fig. 13, top, and is not illustrated here.

Remembering that Refs. [43,44] tabulate the rms estimates of the quadrupole deformations, and thus that the results are by definition positive, we find that for ^{36}Ar, $\alpha_{20}^{\mathrm{exp}} = 0.2573(^{+87}_{-48})$, and for ^{56}Fe, Fig. 13, bottom, $\alpha_{20}^{\mathrm{exp}} = 0.239(2)$, compared with $\alpha_{20}^{\mathrm{th}} \approx -0.20$, and $\alpha_{20}^{\mathrm{th}} \approx +0.19$, respectively, in a very encouraging correspondence.

Let us remark in passing that the results for ^{44}Ti, Fig. 14, bottom, suggest the presence of a triaxial large coexisting deformation ("superdeformation") minimum at $\alpha_{20} \approx 0.47$ and $\gamma \approx \pm 30^\circ$.

In summarizing and concluding this part of the analysis, let us underline the significance of the strong variations ("jumps") in the behavior of the equilibrium deformations accompanying a small modification of the Z or N numbers, rare as compared to the usually observed smooth ("continuous") behavior in heavy and very heavy nuclei. Consequently, generating such structures by the model in which no element was adjusted to reproduce them can be viewed as a strong argument in favor of its prediction capacities. Our calculations provide more evidence of this type; limitation is caused by size constraints.

VI. TOROIDAL AND OTHER EXOTIC-SHAPE CONFIGURATIONS IN $A \approx$ (30–50) NUCLEI

The results for single-particle energies of protons and neutrons in the mass range discussed in this article, Fig. 9, suggest possible presence of very strongly deformed oblate and prolate equilibrium shapes. The strongest gaps correspond to proton/neutron numbers $Z, N = 14$ and 16, which may combine with the neutron/proton numbers $N, Z = 26$ and 28.

As mentioned earlier, the potential energy surfaces of the relatively light nuclei discussed in this article vary in a *remarkably strong manner* when the nucleon numbers change even by a few (e.g., ΔN or $\Delta Z = 2$) units. It will be practical to adapt the presentation to this property.

A. Presenting extreme-shape coexistence scenarios: $A \approx 30$ mass range

Let us begin by illustrating potential energy surfaces for the nuclei with the largest single-nucleon energy gaps visible in Fig. 9, i.e., for $Z, N = 14$ and 16. It turns out that the strongest shell versus deformation effects occur as the result of the combination of the axial quadrupole and hexadecapole deformations, α_{20} and α_{40}; cf. Figs. 15–17.

There occur four types of competing minima with extreme deformations, all typical for this mass range. We refer to these minima as superdeformed prolate and superdeformed oblate as well as toroidal and hyperdeformed. The implied shapes (Figs. 18–21) can be characterized as follows:

(1) Extreme negative hexadecapole-deformation dominated minima with α_{40} varying down to as much as $\alpha_{40} \approx -0.60$ or so, combined with quadrupole oblate shape deformation within the range $\alpha_{20} \in [-0.50, -0.25]$; cf. maps for $^{28-30}$Si and ^{32}S in Figs. 15–17 and shapes in Fig. 18.

(2) Extreme prolate-shape dominated minima, often qualified as superdeformed with $\alpha_{20} \in [0.60, 0.70]$. Unlike the analogous configurations in rare earth nuclei, this elongation is accompanied by an extreme, negative hexadecapole deformation at the level of $\alpha_{40} \approx -0.40$

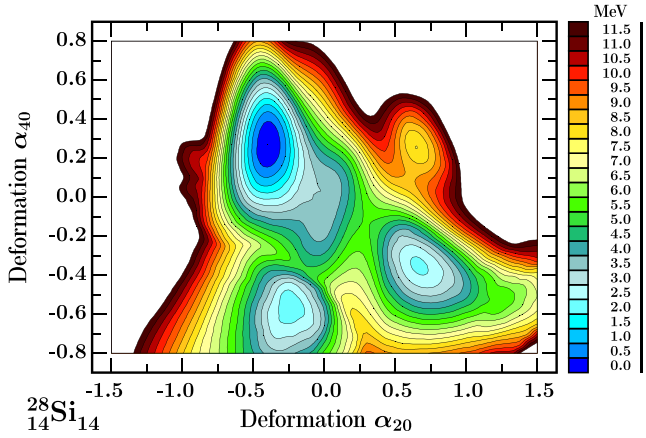

FIG. 15. Total energy α_{40} vs α_{20} projection for ^{28}Si; observe pronounced shape coexistence and strong separating barriers.

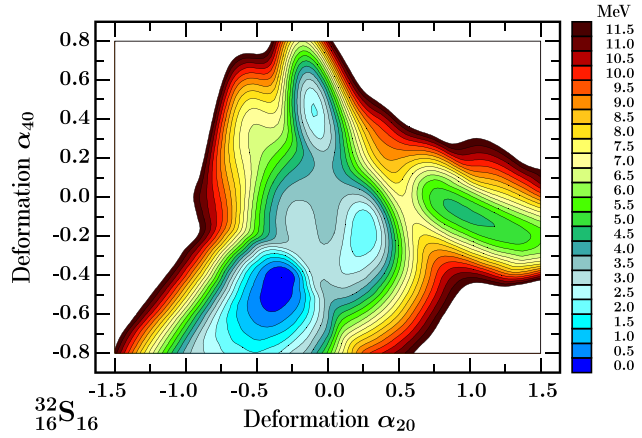

FIG. 17. Similar to the preceding illustration but for ^{32}S.

(cf. energy minimum for ^{28}Si in Fig. 15), whereas the corresponding nuclear surface is illustrated in Fig. 19.

(3) Strong positive hexadecapole deformation in the range $\alpha_{40} \in [0.30, 0.40]$ superposed with oblate down to superoblate quadrupole components with $\alpha_{20} \in [-0.50, -0.30]$ visible for ^{28}Si and ^{32}S in Figs. 15 and 17; a typical corresponding surface can be seen in Fig. 20.

(4) Hyperdeformed elongated shapes corresponding to relatively highly exited secondary minimum at $\alpha_{20} \approx 1$ and some small α_{40} component; cf. the map for ^{32}S in Fig. 17 and nuclear surface illustrated in Fig. 21.

It turns out that due to the extreme similarity between the proton and neutron single-nucleon energy spectra the potential energy surfaces of $^{30}_{14}Si_{16}$ and $^{30}_{16}S_{14}$ are very similar as well and thus the latter is not shown.

B. Nuclear toroidal geometry: About evolution of concepts, methods, and goals

Since an important part of the discussion in this section addresses nuclear configurations which we call toroidal-like—or simply toroidal—it will be instructive to interrupt shortly the presentation of our theoretical predictions related to the shape coexistence in light nuclei by a brief account of the previously published information on the subject.

Notice that combinations of extreme axially symmetric quadrupole and hexadecapole deformations introduced here are rather atypical and seldom illustrated in the literature but at the same time lead to very exotic nuclear shapes. This is also why we provide the corresponding geometrical representations in Figs. 18 to 21.

The hypothesis of existence in nature of toroidal nuclei attracted attention of various authors for some time. The definition of toroidal geometry used was usually different from the one adopted in the present article, which is more relaxed. Most often, toroidal geometry was introduced by parametrizing the form of the torus ("ring-like shape") with the help of its inner and outer radii, alternatively the torus radius R. The so-defined surface possesses a certain parametric freedom, which in turn allows us to study some shape variations. These can be used in applications in, e.g., macroscopic energy models or as constraining relations in the self-consistent iterative approaches and constructing the potential energy surfaces.

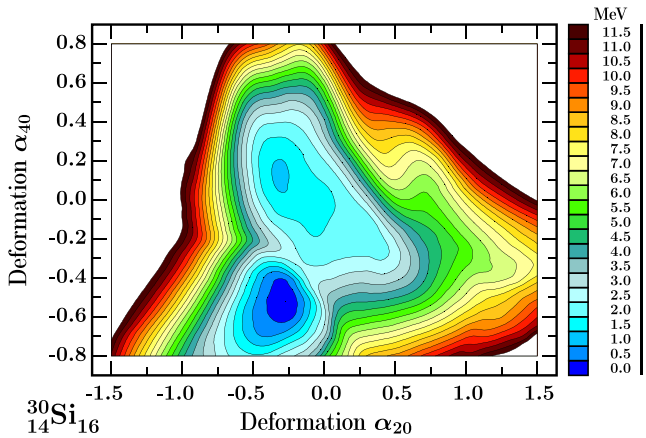

FIG. 16. Similar to the preceding illustration but for ^{30}Si.

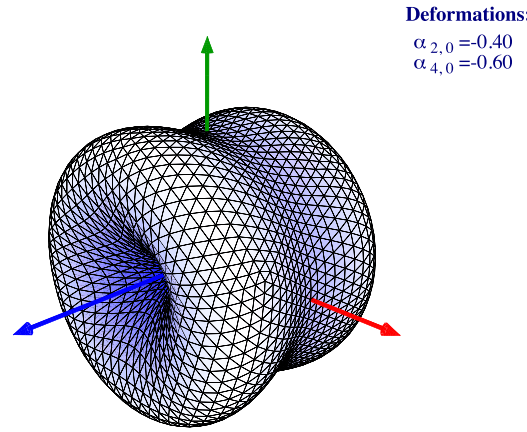

FIG. 18. Nuclear shapes typical for negative super-hexadecapole minima as in the case of $^{28–30}$Si and ^{32}S of Figs. 15–17, here referred to as toroidal.

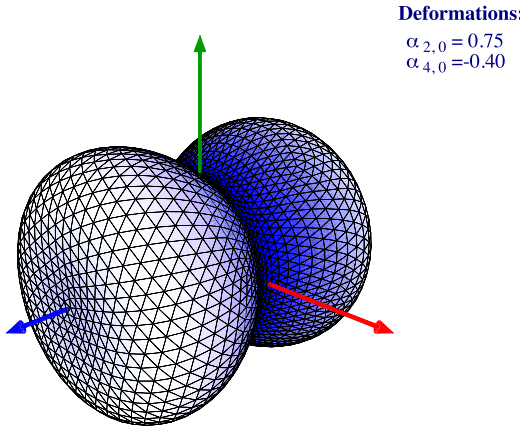

FIG. 19. Illustration of nuclear surface corresponding to the superdeformed minimum of ^{28}Si from Fig. 15.

This type of an approach, as any other approach involving predefined surfaces treated as nuclear surfaces, can only be seen as an approximation of a realistic nuclear geometry. Any real many-nucleon system can hardly be expected to respect strictly any predefined geometry. Moreover, let us emphasize that the nuclear mean-field theory can only be treated as the first-step approximation allowing us to calculate the static nuclear potential energy surfaces as functions of *deformation parameters*, the latter playing a role of (usually a few) collective variables representing all the A nucleons simultaneously.

Consequently, in order to obtain further experiment-comparable observables such as collective excitations of either vibrational or rotational character and related electromagnetic transition probabilities, the corresponding collective theory (often referred to as "Bohr model") should be applied. This brings us to the notion of the collective wave functions with the related notion of the zero-point oscillations and shape probability distributions and thus the classes of nuclear geometries much richer than the originally predefined starting shape geometry, e.g., that of the toroid defined as ringlike object. At the same time, the density distributions obtained via

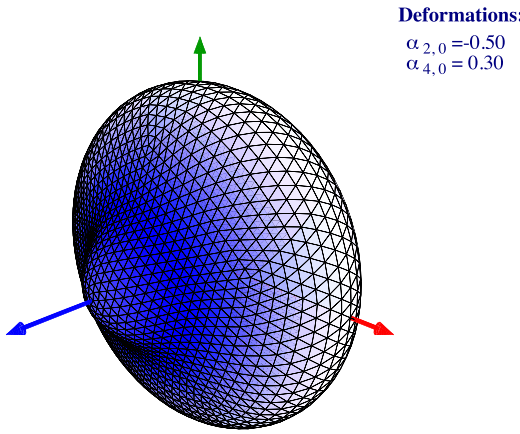

FIG. 20. Similar to the preceding one but typical for positive strong-hexadecapole deformations as in the case of $^{28-30}$Si and ^{32}S of Figs. 15–17.

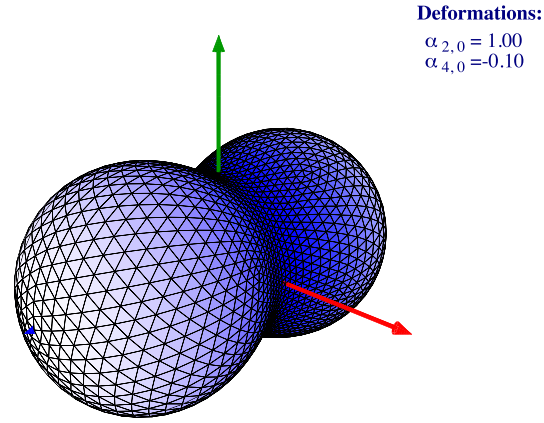

FIG. 21. Hyperdeformed shape expected to accompany an excited shape isomer in ^{32}S; cf. Fig. 17.

self-consistent iterative methods might resemble the ringlike distributions only to a very limited extent.

In this article, we use the notion of nuclear surfaces Σ, defined through Eq. (3) by employing the *basis* of the spherical harmonics. The latter allow—at least in principle—for arbitrarily extended summations which may include infinity of terms and thus any possible shape. Consequently, the just-mentioned torus-shape definitions employing two specific parameters can be seen (at least in principle) as a particular case of the general relation (3). In the present article, we profit from the fact that already two deformation parameters, α_{20} and sufficiently large, negative α_{40}, lead to ringlike geometry; cf. Fig. 18. It should be emphasized that a variation of the two parameters leads to a certain elasticity of the resulting toroid-like shapes, which might resemble the ones in Fig. 18, but may also deviate significantly while preserving the condition of vanishing density near the symmetry axis and close to the center of the nucleus.

Importantly, and thanks to the parametric freedom provided by the expansion in Eq. (3), we were able to test the stability of the obtained toroid-like equilibrium shapes, which correspond to the potential energy minima with strongly negative α_{40} visible in the illustrations of this article. This has been done by introducing several 3D combination of the deformation parameters including triaxiality parameter α_{22} with the corresponding 3D mesh spanned by the variables $\{\alpha_{20}, \alpha_{22}, \alpha_{40}\}$, as well as the octupole-type instabilities of the type $\{\alpha_{20}, \alpha_{3,\mu}, \alpha_{40}\}$ for $\mu = 0, 1, 2, 3$ and hexadecapole-type instabilities $\{\alpha_{20}, \alpha_{40}, \alpha_{4,\mu}\}$ with $\mu = 1, 2, 3, 4$. The corresponding results do not impact the conclusions of this article about the presence of the toroid-like configurations, but enrich the class of possible predictions, e.g., in terms of low-lying collective vibrations; this type of effects will be published elsewhere.

Finally let us mention that, semantics apart, the toroidal-like axially symmetric nuclear shapes with the mass distribution strongly lowered along the symmetry axis and close to the nuclear center appear in the present calculations in *competition* with other configurations, in particular the ones with deformations comparable with the existing experimental data, within common potential energy surfaces. This allows,

for instance, performing the calculations of the probabilities of transmission through the potential barriers separating various minima in full analogy to the calculations of the fission probabilities and advance the studies of the instability properties and/or the issue of the partial lifetimes, etc.

Among the articles addressing specifically the physics of nuclei with ringlike geometry, let us mention Refs. [46–48] focusing on toroidal, toroidal and bubble, and rotating toroidal nuclei, respectively, followed by an extended discussion of the properties of the corresponding hot nuclei in Refs. [49,50]. Some studies addressed the issue of formation and decay of toroidal nuclei, in particular via multifragmentation; cf. Refs. [51,52]. Another direction of research addresses the criteria of identification via rotational and/or isomer properties; cf., e.g., Refs. [53,54]. Argumentations formulated more recently employ the idea of profiting from axial symmetry of the configurations in question, expected to generate isomers referred to as high-K isomers. Calculations of this type can be found, e.g., in Refs. [55–57].

C. Nuclei in the $A \approx$ (40–50) mass range

The oblate shape gaps at $Z = N = 14$ and analogously at $Z = N = 26$ discussed in relation to Fig. 9 can be considered *huge in the scale of the whole mass table,* given the fact that they exceed by a couple of MeV the corresponding spherical gaps, the latter usually considered dominating the nuclear shell structure. These shell effects contribute to the phenomenological macroscopic-microscopic total energy formula together with the pairing corrections on top of the macroscopic energy expression with a relatively complex dependence on Z and N. In medium-heavy and heavy nuclei, this complex dependence is often regular, generating potential energy surfaces of considerable similitude. Fortunately, as already noticed in the preceding sections, in the discussed mass range, the differences from neighbor to neighbor are significant and we keep emphasizing this mechanism in what follows to strengthen the arguments in favor of predictive power of the approach used.

We proceed discussing the effects of the oblate shape gaps at $Z = N = 14$ and analogously at $Z = N = 26$ beginning with ^{38,40}Si. As illustrated in Figs. 22–25, strong negative hexadecapole deformation effects are present at $N = 24$, whereas at $N = 28$ (not shown) the spherical shell-closure dominates. It follows that in the potential energy surface of the nucleus $^{38}_{14}Si_{24}$, a normal-deformed ground-state minimum at $\alpha_{20}^{\rm th} \approx 0.23$ is accompanied by the secondary oblate toroidal symmetry minimum with $\alpha_{20}^{\rm th} \approx -0.45$. The latter nucleus is the heaviest isotope of silicon for which the mean quadrupole equilibrium deformation has been measured; cf. Ref. [43]. The corresponding result $\alpha_{20}^{\rm exp} = 0.249(48)$ is in excellent correspondence with the static minimum visible from Fig. 22.

Whereas the ground-state quadrupole deformation in ^{38}Si, $\alpha_{20}^{\rm th} \approx 0.23$, can be considered normal, the result for ^{40}Si, Fig. 23, with $\alpha_{20}^{\rm th} \approx -0.45$ can be qualified as superoblate. The strongest similitude between two neighboring nuclei can be seen by comparing total energy landscapes of ^{40}S, Fig. 24, and ^{42}S, Fig. 25. The experimental value for the rms ground-state deformation in ^{40}Si, after Ref. [44], is $\alpha_{20}^{\rm exp} \approx 0.37(5)$,

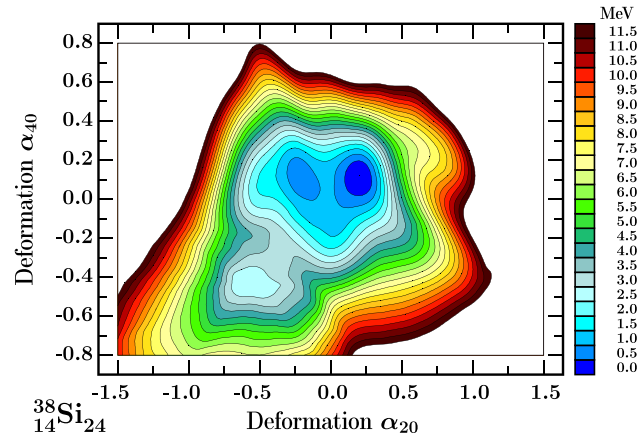

FIG. 22. Potential energy for ^{38}Si with shape coexistence between a normal-deformed prolate ground-state minimum at $\alpha_{20}^{\rm th} \approx 0.23$ and $\alpha_{40}^{\rm th} \approx 0.10$ and a superoblate toroidal symmetry minimum at $\alpha_{20}^{\rm th} \approx -0.50$ and $\alpha_{40}^{\rm th} \approx -0.50$, the latter with the shape close to the one illustrated in Fig. 18. Let us emphasize that the experimental equilibrium rms average $\alpha_{20}^{\rm exp} = 0.255(47)$ is in excellent agreement with the predicted value for the ground state with $\alpha_{20}^{\rm th} \approx 0.23$.

in very close correspondence to the model prediction $\alpha_{20}^{\rm th} \approx -0.40$, up to the sign of the experimental deformation which remains unknown.

Let us emphasize that, compared to the preceding two cases illustrated, the prediction for ^{40}S excitation energy of the toroidal isomeric minimum of only about 0.5 MeV above the ground-state indicates that such a state is very likely easier to populate experimentally.

The observed correspondence between experimental results and modeling encourages thinking that the predicted shape coexistence involving exotic toroidal symmetry

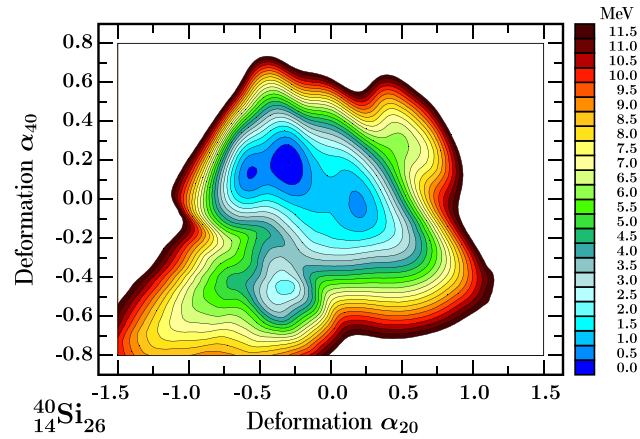

FIG. 23. Similar to the preceding one but for nucleus ^{40}Si. The ground-state minimum corresponds to superoblate shape at $\alpha_{20}^{\rm th} \approx -0.45$ and $\alpha_{40}^{\rm th} \approx 0.20$, whereas the secondary coexisting minimum is predicted at $\alpha_{20}^{\rm th} \approx -0.45$ and $\alpha_{40}^{\rm th} \approx -0.50$, thus resembling toroidal symmetry illustrated in Fig. 18. The experimental value for the rms ground-state deformation after Ref. [44] is $\alpha_{20}^{\rm exp} \approx 0.37(5)$ in very close correspondence to the model prediction up to the sign of the deformation which remains experimentally unknown.

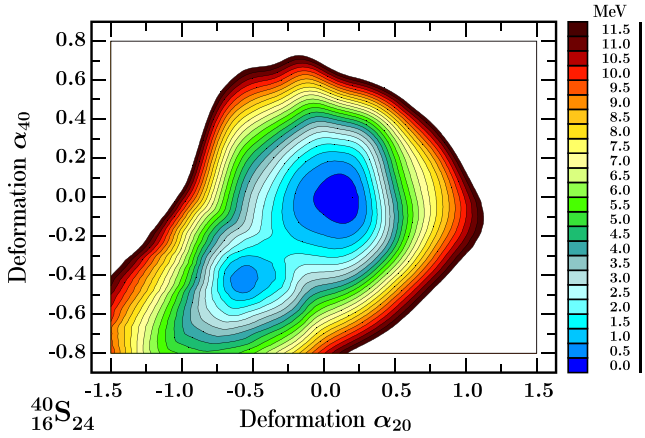

FIG. 24. Potential energy for ^{40}S showing shape coexistence between a normal-deformed prolate minimum with $\alpha_{20}^{\rm th} \approx 0.23$ and $\alpha_{40}^{\rm th} \approx 0$ and a superoblate toroidal symmetry minimum at $\alpha_{20}^{\rm th} \approx -0.60$ and $\alpha_{40}^{\rm th} \approx -0.45$, with separating barrier of the order of 2 MeV; cf. Fig. 18 for the shape illustration. After Ref. [44], the rms ground-state deformation is $\alpha_{20}^{\rm exp} \approx 0.284(15)$ compared with the model prediction of $\alpha_{20}^{\rm th} \approx 0.23$.

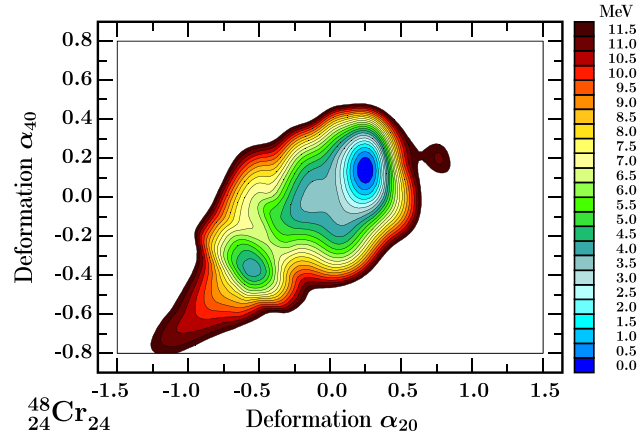

FIG. 26. Total energy projection on the $(\alpha_{20}, \alpha_{40})$ plane for $Z = N$ nucleus $^{48}_{24}$Cr$_{24}$. Perhaps paradoxically, there are no significant $Z = N = 24$ single-particle energy spacings in Fig. 9, for $\alpha_{22} < 0$, and yet the toroidal symmetry configuration is well pronounced due to the α_{40}-deformation impact. After Ref. [44], the experimental average ground-state equilibrium deformation is $\alpha_{20}^{\rm exp} = 0.340(19)$. For comparison, the static minimum deformation $\alpha_{20}^{\rm th} \approx 0.28$.

configurations in these and a few neighboring nuclei is trustworthy, thus stimulating experimental identification efforts. Detailed analysis of the corresponding properties is in progress and will be presented elsewhere.

To complete the discussion of the extreme-oblate deformation structures, let us present two $Z = N$ nuclei in the mass $A \approx 50$ range: $^{48}_{24}$Cr$_{24}$ and $^{52}_{26}$Fe$_{26}$, with the potential energy surfaces illustrated in Figs. 26 and 27, respectively. Both can be considered in a way unusual even though for totally different reasons.

The nucleus ^{52}Fe can, according to the present calculations, be considered more magic than the doubly magic $^{56}_{28}$Ni$_{28}$. This phrasing is justified by the fact that the realistic mean-field estimates give for the gap sizes $\delta e_{Z,N=28} \approx 4$ MeV at spherical shape compared with $\delta e_{Z,N=26} \approx 7$ MeV at the super-(hyper)-oblate shapes with $\alpha_{20} \sim -0.75$; cf. Fig. 9 and the shape illustration in Fig. 28. The deformed shell effects of these proportions are unique in the scale of the whole mass table.

The reason for considering the shape properties of ^{48}Cr as atypical, yet extreme, is the fact that its potential energy surface, Fig. 26, manifests superoblate flattening at $\alpha_{20} < -0.50$, whereas there are no remarkable level spacing at all at $Z = N = 24$ visible from Fig. 9. The underlying reasons for this atypical relation are that, first, there is a significant shell structure evolution with hexadecapole deformation approaching

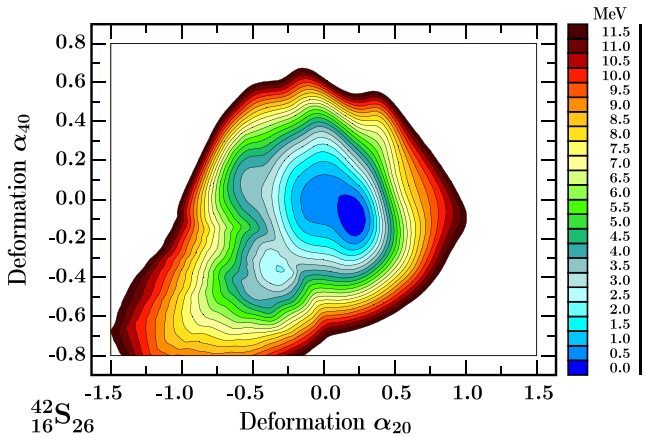

FIG. 25. Similar to the preceding one but for ^{42}S. The prolate ground-state minimum is well pronounced, deformation $\alpha_{20}^{\rm th} \approx 0.25$ compared to $\alpha_{20}^{\rm exp} \approx 0.300(24)$, whereas the toroidal excited minimum lies about 2.5 MeV higher, with the separation barrier between the two of about 1 MeV; the barriers of this order of magnitude may not be sufficient to stabilize the related minimum against zero-point oscillations.

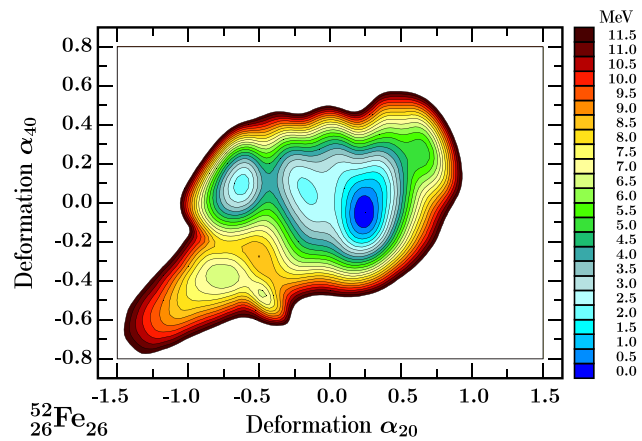

FIG. 27. Total energy projection on the $(\alpha_{20}, \alpha_{40})$ plane for $Z = N$ nucleus $^{52}_{26}$Fe$_{26}$. After Ref. [44], the experimental average ground-state equilibrium deformation is $\alpha_{20}^{\rm exp} = 0.230(14)$ in correspondence with the static deformation $\alpha_{20}^{\rm th} \approx 0.25$. The minima at deformations $\alpha_{20} \approx -0.7$ and $\alpha_{40} \approx 0$ are sometimes qualified as hyperoblate; cf. illustration in Fig. 28.

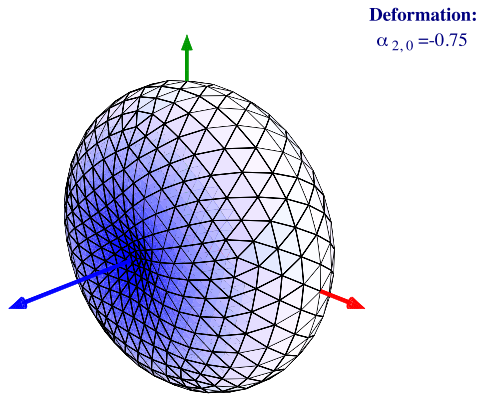

FIG. 28. Illustration of the hyperoblate shape corresponding to $\alpha_{20} \approx -0.7$, representative for the most extreme oblate configurations ^{52}Fe nucleus; see the text for further comments.

$\alpha_{40} \approx -0.40$, and second, that the Strutinsky shell energies remain (sometimes significantly) negative in the direct neighborhood of the strong shell gaps, here at $Z = N = 26$.

D. Remarks about toroidal yrast-trap and *K* isomers as means of experimental identification

The fact that a toroidal symmetry configuration possesses axial symmetry implies that the projections m_n of the individual-nucleonic angular momenta j_n on the symmetry (say $\mathcal{O}_z$) axis—as well as the projection K of the total angular momentum I—are conserved. Since according to elementary quantum mechanics principles, collective rotation about the symmetry axis is not allowed, the corresponding excitation E versus I pattern is determined by particle-hole excitations. The excitation energies are constructed out of differences among the single-nucleonic mean-field energies and, since the latter form no specific regularities, the resulting total energies are strongly irregular, in particular as functions of increasing total angular momentum of the nucleus. As a result, the yrast-line energies do not form monotonic sequences [in contrast to rotational bands with regularly increasing $E_I \propto I(I+1)$].

It follows that several specific spin values may occur (we refer to them as $I_{\rm trap}$), such that

$$E_{I_{\rm trap}-1} \geqslant E_{I_{\rm trap}} \quad \text{and} \quad E_{I_{\rm trap}-2} \geqslant E_{I_{\rm trap}}. \tag{29}$$

In other words, the indicated sequence of three energies forms a "spin pocket" usually called a *yrast trap*. Such a state could decay via electric or magnetic octupole $\Delta I = 3$ transitions, under the condition that $E_{I_{\rm trap}} \geqslant E_{I_{\rm trap}-3}$. This in itself implies a hindrance at the level of several orders of magnitude, with the corresponding *single-particle* strength, and the corresponding configuration would very likely become isomeric.

But the *single particle-strength hindrance factors*, already very strong, are to be expected relatively seldom, and only if the structural rearrangements corresponding to such transitions are of the one-particle one-hole format. Indeed, due to strong irregularity of the single-nucleon energy patterns, the configurations underlying the states close in energy and spin are often very different, involving n-particle n-hole rearrangements, with $n = 2, 3, 4 \ldots$. As a consequence, we should expect the presence of numerous isomers with even higher probability.

However, the just-mentioned mechanism of the hindrance due to strong structural differences between the initial and final states may cause isomerism even without the energy pocket-type structures. Indeed, very different structures of the states corresponding to the initial value $I_{\rm in}$ and the values $I = I_{\rm in} - 1$, $I = I_{\rm in} - 2$, etc., will result with very similar retardation effects, thus encouraging even more strongly the experimental verification of a presence of toroidal structures in nature via isomer search.

Results of the present article indicate implicitly that employing K isomers and yrast traps as means of identification of toroidal structures might be complicated by the fact that toroidal structures are predicted to be accompanied by at least one—and sometimes two—competing axial symmetry minima. Each of those will generate its own family of trap or K isomers with the corresponding competing decay schemes and isomeric sequences and thus the experimental analysis will need to be appropriately designed.

A helpful indication about how to refine experimental analysis in this context is provided by the fact that the shapes and the implied nuclear density distributions in the toroidal versus slightly oblate of prolate ones are significantly different. This implies in turn that the toroidal decay scheme is not going to "communicate" with, e.g., moderately oblate-configuration decay schemes with transitions of strengths comparable to the strengths of the intrasequence decay transitions. The justification of the last statement has to do with the potential barrier penetrability and is analogous to the arguments used to calculate the transition probabilities between the secondary (fission isomeric) minima and the the ground-state minima.

In concluding this section, let us emphasize that exploiting the axial symmetry of the toroidal structures which necessarily generate the presence of the trap and other K isomers encourages employing adapted instrumentation. Such an instrumentation should optimally involve the contemporary γ-detection systems as well as the high-resolution mass spectrometers.

VII. SUMMARY AND CONCLUDING REMARKS

In this article, we used the nuclear mean-field approach in the realization employing phenomenological Woods-Saxon Hamiltonian with the parametrization referred to as universal. The corresponding Hamiltonian depends *a priori* on 12 adjustable parameters, six for the protons and neutrons each. In our parameter adjustment procedure, we used the experimental single nucleon energies of the following eight doubly magic spherical nuclei: ^{16}O, ^{40}Ca, ^{48}Ca, ^{56}Ni, ^{90}Zr, ^{132}Sn, ^{146}Gd, and ^{208}Pb. The energies in question were determined by other authors.

We employed the standard methods of the inverse problem theory of applied mathematics with the help of which we established the presence of parametric correlations among the original 12 parameters. As it turns out, the central potential radius parameter and the central potential depth parameter

are to a good approximation linearly correlated, and independently for the neutrons and protons. Similar independent correlations exist between the spin-orbit radius and strength parameters for protons and neutrons. In this way, we arrived at determining four one-to-one correlations which decrease the number of independent adjustment parameters from 12 originally to eight.

Having optimized the description of the single nucleon energies in *spherical* doubly magic nuclei, we proceeded to cross-checking the theory predictions for the ground-state equilibrium deformations in numerous *deformed* nuclei in the studied region, for which experimental data about average quadrupole deformations exist in the literature. The credibility of this type of test significantly increases due to the fact that in the light nuclei studied, the experimental values of the equilibrium deformations often vary very irregularly when increasing the nucleon number even just by two units—and this for no obvious known reasons. Comparison shows an approximate correspondence at the level of $\pm 15\%$ accuracy including irregularities. Since no element in the parameter adjustment was fitted to irregularities mentioned, a reproduction of this type of jumps by the model can be interpreted as affirmative test of its predictive power.

As the next step, we performed systematic calculations of the potential energy surfaces primarily in the space including quadrupole deformation parameters α_{20} and α_{22} [equivalently (β, γ)] and hexadecapole deformation α_{40} and including some extra stability tests engaging $\alpha_{4\mu\neq 0}$ as well as octupole ones with $\alpha_{3\mu}$ for $\mu = 0, 1, 2$, and 3.

Our calculations suggest the presence of the shell gaps which appear at the superdeformed oblate shapes and are 2–3 MeV larger than the corresponding spherical shell gaps usually considered dominating the nuclear shell structure. The gaps in question correspond to the nucleon numbers $N, Z = 14$ (approximately 6 MeV at $\alpha_{20} \approx -0.6$ compared with 4.5 MeV at spherical shape) and $N, Z = 26$ (approximately 5 MeV at $\alpha_{20} \approx -0.7$ compared with the largest neighbor gap at $N, Z = 28$ of about 3.5 MeV at spherical shape). These structures result in well-pronounced superoblate and toroidal potential energy minima in the corresponding nuclei in the $A \approx 30$ mass range but also in the vicinities of $A \approx 40$ and $A \approx 50$ mass numbers as discussed in detail in this article.

The predicted exotic toroidal and superoblate configurations mentioned are axially symmetric, which implies the very likely presence of excited particle-hole configurations leading to the mechanism of K isomers. The discussion of the exotic symmetry properties in the present article was limited, for reasons of space limitations, to even-even nuclei only. Needless to say, the extension of those considerations to the odd-even and odd-odd nuclei increases considerably the number of candidate cases for the possible experimental identification studies.

In our approach, we use consistently the expansion of the nuclear surface in terms of the spherical harmonic basis and the toroidal-like axial symmetry minima appear as a part of the shape competition and coexistence between at least two, often three, axial symmetry minima. These minima coexist within regular, continuous potential energy surfaces which allows us to obtain simultaneously the potential energy barriers between them and investigate the hindrance factors accompanying interminimum transitions via barrier penetration mechanism.

This observation has very important consequences.

First, it implies that using the yrast trap and K isomers built on top of the toroidal, axial symmetry structures for identifying toroidal nuclei is complicated because these nuclei produce two or three families of isomeric and decay sequences, each of which are associated with their original shape-coexisting configuration.

Fortunately, one should expect that each of the discussed shape configurations should produce its own decay sequence with their isomers decaying preferentially within the sequence (intrasequential decay) since the potential penetration mechanisms just mentioned should provide strong hindrances for extrasequence transitions.

On the other hand, the isomeric configurations may give rise to the collective rotational bands about an axis perpendicular to the symmetry axis. Such a mechanism can become a useful contribution on the way toward an identification of the underlying distinct shapes under the condition that the corresponding effective moments of inertia are sufficiently distinct. From the modeling side, the mean-field theory tools are often realistic enough to provide some helpful indications, but population of rotational bands on top of the toroidal-isomeric configurations remains an experimental challenge.

Given expected experimental challenges with populating the collective rotational bands in question, one should envisage population and identification of as many isomers as possible together with their lifetimes, population, and decay patterns. The decay of isomers within a given decay path associated with a given underlying total energy minimum could be analyzed using the usual techniques used to study noncollective decay schemes and there exist powerful theory methods to help in the interpretation of the results of this type.

The approach presented in this article allows us to calculate potential barriers within realistic model conditions. All the competing minima appear associated with the common potential energy surface. This facilitates applying methods used to calculate, e.g., the fission barrier penetrabilities and the associated lifetimes, and we can envisage employing such an approach in the context of an identification of toroidal states.

ACKNOWLEDGMENTS

One of the authors, J.D., acknowledges partial support by the Polish National Science Centre under Contract No. 2016/21/B/ST2/01227. H.-L.W. acknowledges partial support via National Natural Science Foundation of China (Grant No. 11975209) and Physics Research and Development Program of Zhengzhou University (Grant No. 32410017).

[1] J. P. Elliott, Proc. R. Soc. Lond. A **245**, 128 (1958).
[2] J. P. Elliott, Proc. R. Soc. Lond. A **245**, 562 (1958).
[3] M. Brack, J. Damgaard, A. S. Jensen, H. C. Pauli, V. M. Strutinsky, and C. Y. Wong, Rev. Mod. Phys. **44**, 320 (1972).
[4] P. J. Twin, B. M. Nyakó, A. H. Nelson, J. Simpson, M. A. Bentley, H. W. Cranmer-Gordon, P. D. Forsyth, D. Howe, A. R. Mokhtar, J. D. Morrison, J. F. Sharpey-Schafer, and G. Sletten, Phys. Rev. Lett. **57**, 811 (1986).
[5] J. Dudek and W. Nazarewicz, Phys. Rev. C **31**, 298 (1985).
[6] R. D. Ratnaraju, J. P. Draayer, and K. T. Hecht, Nucl. Phys. A **202**, 433 (1973).
[7] K. T. Hecht, *Proceedings of the 15th Solvay Conference on Physics*, 1970 (Gordon and Breach, New York, 1974), pp. 301–329.
[8] J. P. Draayer and K. J. Weeks, Phys. Rev. Lett. **51**, 1422 (1983).
[9] J. P. Draayer and K. J. Weeks, Ann. Phys. (NY) **156**, 41 (1984).
[10] J. Dudek, W. Nazarewicz, Z. Szymański, and G. A. Leander, Phys. Rev. Lett. **59**, 1405 (1987).
[11] X.-L. Han and C.-L. Wu, At. Data Nucl. Data Tables **73**, 43 (1999).
[12] A. Bohr and B. R. Mottelson, *Nuclear Structure* (Benjamin, Reading, MA, 1975), Vol. 2.
[13] I. Hamamoto, Phys. Rev. C **89**, 057301 (2014).
[14] M. Stanoiu, F. Azaiez, Zs. Dombrád, O. Sorlin, B. A. Brown, M. Belleguic, D. Sohler, M. G. Saint Laurent, M. J. Lopez-Jimenez, Y. E. Penionzhkevich *et al.*, Phys. Rev. C **69**, 034312 (2004).
[15] J. Dudek, D. Curien, I. Dedes, K. Mazurek, S. Tagami, Y. R. Shimizu, and T. Bhattacharjee, Phys. Rev. C **97**, 021302(R) (2018).
[16] The universal Woods-Saxon Hamiltonian and associated universal parametrization have been developed in a series of articles: J. Dudek and T. Werner, J. Phys. G: Nucl. Phys. **4**, 1543 (1978); J. Dudek, A. Majhofer, J. Skalski, T. Werner, S. Cwiok, and W. Nazarewicz, *ibid.* **5**, 1359 (1979); J. Dudek, W. Nazarewicz, and T. Werner, Nucl. Phys. A **341**, 253 (1980); J. Dudek, Z. Szymański, and T. Werner, Phys. Rev. C **23**, 920 (1981); and has been summarized in; S. Ćwiok, J. Dudek, W. Nazarewicz, J. Skalski, and T. Werner, Comput. Phys. Commun. **46**, 379 (1987). This approach is being used without modifications by many authors also today.
[17] To illustrate of the use frequency of the universal Woods-Saxon phenomenological mean-field Hamiltonian, we quote below the articles which appeared only in one year (2013) and only in one journal: J. Rissanen, R. M. Clark, K. E. Gregorich, J. M. Gates, C. M. Campbell, H. L. Crawford *et al.*, Phys. Rev. C **88**, 044313 (2013); W. Brodziński and J. Skalski, *ibid.* **88**, 044307 (2013); S. Lalkovski, A. M. Bruce, A. M. Denis Bacelar, M. Górska, S. Pietri, Z. Podolyak *et al.*, *ibid.* **88**, 024302 (2013); H. L. Liu and F. R. Xu, *ibid.* **87**, 067304 (2013); D. S. Delion and R. J. Liotta, *ibid.* **87**, 041302(R) (2013); D. S. Delion, R. J. Liotta, and R. Wyss, *ibid.* **87**, 034328 (2013); D. S. Delion and J. Suhonen, *ibid.* **87**, 024309 (2013); D. Deleanu, D. L. Balabanski, Ts. Venkova, D. Bucurescu, N. Mărginean, E. Ganioğlu, Gh. Căta-Danil, L. Atanasova, I. Căta-Danil, P. Detistov *et al.*, *ibid.* **87**, 014329 (2013).
[18] V. M. Strutinsky, Nucl. Phys. A **95**, 420 (1967); **122**, 1 (1968).
[19] H. J. Krappe, J. R. Nix, and A. J. Sierk, Phys. Rev. C **20**, 992 (1979).
[20] P. Möller and J. R. Nix, Nucl. Phys. A **361**, 117 (1981).
[21] P. Möller and J. R. Nix, At. Data Nucl. Data Tables **26**, 165 (1981).
[22] P. Möller, J. R. Nix, W. D. Myers, and W. J. Swiaątecki, At. Data Nucl. Data Tables **59**, 185 (1995).
[23] M. Bolsterli, E. O. Fiset, J. R. Nix, and J. L. Norton, Phys. Rev. C **5**, 1050 (1972).
[24] W. Satuła, J. Dobaczewski, and W. Nazarewicz, Phys. Rev. Lett. **81**, 3599 (1998).
[25] The domain of the *inverse problem* is served by specialized journals, such as Inverse Problems (IOPP), Journal of Inverse and Ill-Posed Problems (De Gruyter), and Inverse Problems in Science and Engineering (Taylor & Francis).
[26] R. C. Aster, B. Borchers, and C. H. Thurber, *Parameter Estimations and Inverse Problems* (Elsevier, Amsterdam, 2005).
[27] C. R. Vogel, *Computational Methods for Inverse Problem* (Society for Industrial and Applied Mathematics, Philadelphia, 2002).
[28] A. Tarantola, *Inverse Problem Theory and Methods for Model Parameter Estimation* (Society for Industrial and Applied Mathematics, Philadelphia, 2005).
[29] A. Kirsch, *An Introduction to the Mathematical Theory of Inverse Problems*, Applied Mathematical Sciences (Springer, New York, 2005).
[30] A. A. Samarskii and P. N. Vabishchevich, *Numerical Methods for Solving Inverse Problems of Mathematical Physics* (De Gruyter, New York, 2008).
[31] J. Dobaczewski, W. Nazarewicz, and P.-G. Reinhard, J. Phys. G: Nucl. Part. Phys. **41**, 074001 (2014).
[32] J. Piekarewicz, W.-C. Chen, and F. J. Fattoyev, J. Phys. G: Nucl. Part. Phys. **42**, 034018 (2015).
[33] D. G. Ireland and W. Nazarewicz, J. Phys. G: Nucl. Part. Phys. **42**, 030301 (2015), special issue.
[34] J. Dudek, B. Szpak, B. Fornal, and A. Dromard, Phys. Scr. **2013**, 014002 (2013).
[35] J. Dudek, B. Szpak, M.-G. Porquet, and B. Fornal, J. Phys.: Conf. Ser. **267**, 012062 (2011).
[36] B. Szpak, J. Dudek, M.-G. Porquet, and B. Fornal, J. Phys.: Conf. Ser. **267**, 012063 (2011).
[37] J. Dudek, B. Szpak, M.-G. Porquet, H. Molique, K. Rybak, and B. Fornal, J. Phys. G: Nucl. Part. Phys. **37**, 064031 (2010).
[38] J. Dudek, K. Rybak, B. Szpak, M.-G. Porquet, H. Molique, and B. Fornal, Int. J. Mod. Phys. E **19**, 652 (2010).
[39] B. Szpak, J. Dudek, M.-G. Porquet, K. Rybak, H. Molique, and B. Fornal, Int. J. Mod. Phys. E **19**, 665 (2010).
[40] J. Dudek, B. Szpak, A. Dromard, M.-G. Porquet, B. Fornal, and A. Góźź, Int. J. Mod. Phys. E **21**, 1250053 (2012).
[41] I. Dedes and J. Dudek, Acta Phys. Pol. B Proc. Suppl. **10**, 51 (2017).
[42] I. Dedes and J. Dudek, Phys. Scr. **93**, 044003 (2018).
[43] S. Raman, C. W. Nestor Jr., and P. Tikkanen, At. Data Nucl. Data Tables **78**, 1 (2001).
[44] B. Pritychenko, M. Birch, B. Singh, and M. Horoi, At. Data Nucl. Data Tables **107**, 1 (2016).
[45] N. J. Stone, At. Data Nucl. Data Tables **111-112**, 1 (2016).
[46] C. Y. Wong, Phys. Lett. B **41**, 446 (1972).
[47] C. Y. Wong, Ann. Phys. (NY) **77**, 279 (1973).

[48] C. Y. Wong, Phys. Rev. C **17**, 331 (1978).
[49] C. Y. Wong, Phys. Rev. Lett. **55**, 1973 (1985).
[50] J. Y. Zhang and C. Y. Wong, Phys. Rev. C **34**, 1094 (1986).
[51] H. M. Xu, J. B. Natowitz, C. A. Gagliardi, R. E. Tribble, C. Y. Wong, and W. G. Lynch, Phys. Rev. C **48**, 933 (1993).
[52] H. M. Xu, C. A. Gagliardi, R. E. Tribble, and C. Y. Wong, Phys. Rev. C **49**, R1778 (1994).
[53] T. Ichikawa, J. A. Maruhn, N. Itagaki, K. Matsuyanagi, P. G. Reinhard, and S. Ohkubo, Phys. Rev. Lett. **109**, 232503 (2012).
[54] T. Ichikawa, K. Matsuyanagi, J. A. Maruhn, and N. Itagaki, Phys. Rev. C **90**, 034314 (2014).
[55] A. Staszczak and C. Y. Wong, Phys. Lett. B **738**, 401 (2014).
[56] A. Staszczak and C. Y. Wong, Phys. Scr. **90**, 114006 (2015).
[57] A. Staszczak and C. Y. Wong, EPJ Web Conf. **117**, 04008 (2016).